

Deterministic versus Stochastic Optimization for Joint Path Planning and Dynamic Time Splitting in Multiple-UAV-Cached IoT Networks

Trinh Van Chien, *Member, IEEE*, Dinh Thanh Tung, Waqas Khalid, Ngo Cong Dung, Banh Thi Quynh Mai, and Symeon Chatzinotas, *Fellow, IEEE*

Abstract—This paper examines wireless-powered Internet of Things (IoT) networks involving multiple unmanned aerial vehicles (UAVs) equipped with backscatter and caching technologies to relay and transmit signals. For data communication and energy harvesting (EH), the source transmits information and power to UAVs using the dynamic time splitting (DTS) method. UAVs use harvested energy for passive communication (backscatter) and for active communication (transmitting information) to the destination. The primary objective is to maximize the total throughput by jointly optimizing the DTS ratio, trajectory, and transmission power, leveraging the UAVs’ caching capability. This optimization problem is challenging due to its non-convexity. Therefore, an efficient alternating algorithm using the block coordinate descent (BCD) method is proposed to optimize each variable given the fixed values of the other parameters. By applying the Karush-Kuhn-Tucker (KKT) conditions, we derive a closed-form expression for the optimal DTS ratio, significantly reducing computation time. The optimal values for the other two parameters are determined using the BCD. In order to thoroughly assess the effectiveness of various solutions for the original problem, this paper introduces an approach leveraging a genetic algorithm (GA). The GA in this context employs a one-point crossover method, value mutation, and rank-based selection based on fitness values. Numerical results show that the BCD and GA achieve at least 31% throughput improvement over the benchmarks, with reduced computational time. These findings demonstrate the performance gain and practical feasibility of our solutions in caching-enabled UAV-aided IoT networks.

Index Terms—Unmanned aerial vehicle, wireless-powered communication, block coordinate descent, genetic algorithm

I. INTRODUCTION

Unmanned aerial vehicles (UAVs) have become essential in military, civilian, and commercial domains, supporting surveillance, disaster relief, environmental monitoring, and agriculture [1]. Their ability to access harsh locations and quickly collect data across large areas enhances operational efficiency [2], [3]. Technological advancements continue to extend UAVs’ flight duration, payload capacity, and communication range, positioning them as effective tools in wireless

communication. UAVs serve both as relay nodes to counteract signal degradation from shadowing or congested base stations (BSs) [4], and as airborne BSs to restore connectivity during disasters when terrestrial BSs are impaired. Compared to portable ground BSs, UAVs offer faster deployment and resilience to infrastructure failures [5]. Nonetheless, increasing UAV operations introduces challenges related to energy usage and memory limitations. Employing technologies such as backscatter and caching helps mitigate these issues by improving energy conservation and data handling. Recent progress in IoT-enabled UAV systems demonstrates laser-powered backscatter significantly improving EH for extended missions [6]. Furthermore, integrating backscatter with UAV-assisted mobile edge computing has been shown to effectively reduce latency and energy consumption [7].

Backscatter communication (BackCom) addresses energy efficiency in UAV networks using circuits that operate at micro-Watt (μW) power levels [8], [9], [10]. Efficiency is further improved through optimized UAV flight paths, backscatter device (BD) scheduling, and carrier emitter (CE) management [11]. Although transmission requires minimal power, UAV propulsion remains energy-intensive, reaching hundreds of Watts [12], and limited battery storage imposes operational constraints [13]. As a solution, wireless power transfer (WPT) supports continuous UAV activity across diverse applications [14], [15], [16], [17]. Jayakody *et al.* [18] proposed a self-sustaining UAV system by integrating EH, WPT, and simultaneous wireless information and power transfer (SWIPT), resolving self-interference in full-duplex transmission. In another study, Yan *et al.* [19] focused on UAV-enabled wireless sensor networks (WSNs), where UAVs harvested energy from base stations to serve multiple WSNs, optimizing total energy acquisition across sensors. Recent advances have demonstrated UAV-based backscatter systems enabling mobile edge computing for IoT applications with improved success rates [20].

Cache memory plays a critical role in reducing latency and controlling network congestion by storing frequently accessed content near end users [21], [22]. In UAV networks, onboard caching notably improves response time in areas with difficult terrain or limited infrastructure. Deploying caches at edge UAV nodes not only enhances system performance but also addresses latency concerns. Masood *et al.* [23] introduced a content caching scheme for high-altitude platform-assisted multi-UAV systems, employing a hierarchical federated learning algorithm to forecast content demand while ensuring user privacy. Meanwhile, Zhang *et al.* [24] designed a UAV-enabled

Trinh Van Chien, Dinh Thanh Tung, Ngo Cong Dung, and Banh Thi Quynh Mai are with the School of Information and Communications Technology, Hanoi University of Science and Technology, Hanoi 100000, Vietnam (email: chientv@soict.hust.edu.vn). Waqas Khalid is with the Department of Electrical and Electronic Engineering, and the Next Generation Internet of Everything Laboratory (NGIoE Lab), University of Nottingham Ningbo China, Ningbo 315100, China (e-mail: Waqas.Khalid@nottingham.edu.cn). Symeon Chatzinotas is with the Interdisciplinary Centre for Security, Reliability and Trust (SnT), University of Luxembourg, 1855 Luxembourg, Luxembourg (e-mail: symeon.chatzinotas@uni.lu). This research is funded by Hanoi University of Science and Technology (HUST) under project number T2024-PC-039. Corresponding author: Banh Thi Quynh Mai.

TABLE I
BOLDLY CONTRASTING OUR CONTRIBUTION TO THE LITERATURE

Approach	2020 [26]	2022 [27]	2022 [28]	2023 [29]	2024 [30]	2024 [31]	2025 [32]	This paper
Mutiple UAV supported	X	X	✓	X	✓	✓	✓	✓
Backscatter supported	✓	✓	✓	✓	X	X	X	✓
Power allocation	X	X	X	X	X	X	X	✓
Caching mechanism	X	✓	X	X	X	X	X	✓
Fixed altitudes' UAVs	✓	✓	✓	✓	X	X	✓	X
Dynamic altitudes' UAVs	X	X	X	X	✓	X	X	✓
UAV acting as a transmitter	✓	X	✓	✓	X	✓	✓	✓
UAV acting as a backscatter	X	✓	X	X	X	X	X	✓
Evolutionary algorithm supported	X	X	X	X	X	✓	X	✓
DRL supported	X	X	X	X	✓	X	✓	✓

protocol for data dissemination in Vehicle-to-everything systems that merges proactive caching with cooperative file sharing. Their solution leverages dynamic trajectory scheduling to optimize cache duration and applies relay prioritization with channel prediction to increase sharing performance. A recent study has also shown that joint cooperative caching and power control in UAV-enabled IoT vehicular networks significantly improves energy efficiency [25].

Building on previous discussions and highlighting the efficiency of wireless power, caching, and BackCom technologies, this study examines a caching-enabled BackCom network with multiple UAVs equipped with SWIPT capabilities. The UAVs cache frequently requested content, reducing the data transmitted from the source to the destination. In contrast to prior studies in [26], which primarily focus on a single UAV functioning as a transmitter or receiver in 2D space or neglect the total-power optimization, this research addresses a network of UAVs functioning as airborne. These UAVs harvest energy from signals emitted by the source and use it to reflect the signal toward the destination in a 3D environment, effectively enhancing network efficiency. A comparison with previous works is in Table I, and our key contributions are

- 1) We explore a network where a source transmits to a destination in the absence of a direct link, necessitating the assistance of UAVs. We propose a novel wireless-powered UAV communication protocol, incorporating backscatter and cache-assisted technologies, which significantly reduces power consumption while the base station supplies energy to the UAVs.
- 2) The dynamic time splitting (DTS) is employed to divide each UAV empowered by backscatter devices (UBD) movement slots into intervals for EH and data transmission. Hence, DTS ratio, power transmission, and UAV trajectory require careful planning to optimize throughput under energy constraints. The DTS ratio determines harvested energy and data rates, necessitating precise scaling in each time slot.
- 3) The throughput maximization problem subject to the UAV flying time, speed, trajectory, power, and DTS ratio. To address its non-convex nature, the problem is divided into three sub-problems: optimizing the DTS ratio, the trajectory, and the total power while the other variables are fixed. The closed-form DTS solutions derived from KKT conditions reduce computational complexity.

Trajectory and power optimizations are solved using the BCD through successive convex approximation (SCA).

- 4) Alternatively, a GA-based approach is introduced to seek for a better solution. It employs single-point crossover, replacement mutation, and rank-based selection, with fitness scores that assess variables encoded in multi-dimensional vectors updated across iterations.

To explicitly delimit the scope of the proposed optimization framework, it is imperative to clarify its target practical deployment paradigms. Unlike cellular user equipment networks, the proposed algorithms are fundamentally designed for IoT topologies. Typical application scenarios that strictly align with this requirement include post-disaster structural health monitoring, wide-area precision-agriculture sensor networks, and remote industrial data-collection pipelines. The terrestrial IoT sink nodes (acting as end users) are statically deployed at fixed, pre-surveyed Cartesian coordinates. Consequently, the multi-UAV swarm operates as a centralized fleet of dynamic data mules and wireless energy transmitters, leveraging pre-flight, offline-computed optimal mission parameters to efficiently service these stationary nodes.

The rest of this paper is organized as follows. Section II outlines the system model and the problem formulation. Section III details the iterative algorithm for solving the linear EH model in a 3D UAV-enabled BackCom network. Section IV presents the GA-based optimization. Section V provides numerical results, and Section VI concludes the paper.

II. COMMUNICATION SYSTEM AND SIGNAL MODELS

We investigate a network of multiple UAVs operating in 3D space, enhanced by cache technology and backscatter circuitry, as shown in Fig. 1. The BS is located at the source S and the sink node is positioned at the destination D . The coordinates of S and D are fixed at \mathbf{W}_s and \mathbf{W}_d , respectively. We focus on a scenario where data is transmitted from the BS to the destination in a non-line-of-sight (NLoS) environment or under severe fading conditions, and the user is successfully served by the network. Table II lists frequently used symbols together with their meanings for easier reading and reference.

A. UAV Trajectory & Propagation Channel Model

This study focuses on the communication links between the BS and UBDs, and between UBDs and the destination. To

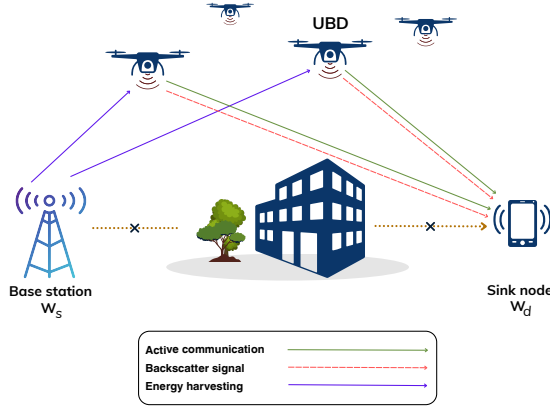


Fig. 1. The considered system model with multiple-UAV trajectory of UAVs.

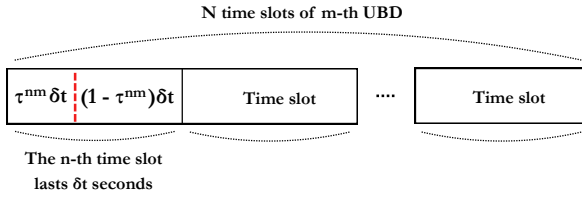


Fig. 2. The schematic time-slot diagram.

provide flexibility for adjustments as the user at D changes location, T is defined as the total duration for a UBD to travel from its initial to final location and serve the destination. The time window T is divided into N slots, each lasting $\delta t = T/N$. Fig. 2 illustrates the microsecond-level synchronization of the DTS protocol within a single optimization epoch T . The continuous block is divided into N discrete slots. Within each slot n , the fraction τ_{nm} is exclusively dedicated to harvesting RF energy from the base station, while the remaining fraction $(1 - \tau_{nm})$ activates the transmitter circuits for backscattering and active data payload delivery to the destination.

The m -th UBD's location during the n -th slot is expressed as \mathbf{q}^{nm} , $\forall n \in \mathcal{N} \triangleq \{0, \dots, N\}$, $m \in \mathcal{M} \triangleq \{1, \dots, M\}$. Representing the maximum UBD speed as V_{\max} , the positions of the m -th UBD, $\forall m \in \mathcal{M}$, between consecutive slots $(n+1)$ and n , $\forall n \in \mathcal{N}$, must satisfy the following constraints

$$\Delta^{nm} \triangleq \|\mathbf{q}^{(n+1)m} - \mathbf{q}^{nm}\| \leq V_{\max} \delta t, \quad (1)$$

$$\mathbf{q}^{0m} = \mathbf{q}^{Im}, \quad \mathbf{q}^{Nm} = \mathbf{q}^{Fm}, \quad (2)$$

where \mathbf{q}^{Im} is the initial location of the m -th UBD; \mathbf{q}^{Fm} is its final location. The constraint (1) requires that the distance covered by the UBD between two successive time slots does not exceed the maximum permissible flight distance within the given time duration δt . Additionally, the constraint (2) imposes that the UBD's trajectory must begin and conclude at the fixed coordinates of points \mathbf{q}^{Im} and \mathbf{q}^{Fm} , respectively. The term $\|\mathbf{q}^{(n+1)m} - \mathbf{q}^{nm}\|$ denotes the Euclidean norm. To maintain consistency in notation, we will refer to the BS, destination, and UBD as s , d , and u , respectively. Thus, $\forall n \in \mathcal{N}$, the distances between the BS and the m -th UBD (for the incoming wave) and between the m -th UBD and the destination (for the

TABLE II
SUMMARY OF KEY NOTATIONS

Symbol	Definition	Unit
K	Total number of UAVs	-
N	Total number of discrete time slots	-
c_r	Redundant content caching ratio	-
τ_{nm}	Dynamic Time Splitting ratio	-
δt	The time interval of each time slot	s
P_{WPT}	Transmission power for Wireless Power Transfer	dB
σ^2	Variance of the Additive White Gaussian Noise	dB
P_s^{nm}	Transmit power of the BS	mW
P_u^{nm}	Transmit power of the UBD	mW
$\mathbf{W}_s, \mathbf{W}_d$	Fixed 3D coordinates of the BS and destination	-
\mathbf{q}^{nm}	The m -th UBD's location during the n -th slot	-

backscattered wave) in the n -th time slot can be expressed as

$$d_{su}^{nm} = \|\mathbf{q}^{nm} - \mathbf{W}_s\|, \quad d_{du}^{nm} = \|\mathbf{q}^{nm} - \mathbf{W}_d\|. \quad (3)$$

In our investigation, a comprehensive fading channel model is considered, incorporating both line-of-sight (LoS) and non-line-of-sight (NLoS) components. This model reflects the deployment of UAVs across diverse radio environments, including rural, urban, and suburban areas. Additionally, we meticulously examine the impact of large-scale and small-scale fading effects to effectively characterize the random fluctuations inherent in the environment [33]. By analyzing the interaction between these factors, we aim to gain a deeper understanding of the complex dynamics and inherent uncertainties governing the fading characteristics of the channels. In the specification, we analyze the network performance relying on the quasi-static fading channel model. Even though the propagation environments vary both in time and frequency, the system operates in coherence intervals during which the channels are static and frequency-flat [34], [35]. Moreover, Rician fading models indicate the presence of dominant LoS components and rich scattering environments, such as in urban areas [36]. The channel coefficient h_{iu}^{nm} for m -th UB, $\forall i \in \{s, d\}$, during the n -th time slot, is given by

$$h_{iu}^{nm} = \sqrt{\psi_{iu}^{nm} \tilde{h}_{iu}^{nm}} = \sqrt{\omega_0 (d_{iu}^{nm})^{-\alpha} \tilde{h}_{iu}^{nm}}, \quad (4)$$

where ψ_{iu}^{nm} and \tilde{h}_{iu}^{nm} represent the symbols for large-scale fading and small-scale fading, respectively, in the n -th time slot. Here, ω_0 is the reference channel gain with d_{iu}^{nm} equal to one meter, and α represents the path loss exponent. The small-scale fading component \tilde{h}_{iu}^{nm} can be expressed as:

$$\tilde{h}_{iu}^{nm} = \sqrt{\frac{K}{1+K}} \bar{h}_{iu}^{nm} + \sqrt{\frac{1}{1+K}} \hat{h}_{iu}^{nm}, \quad (5)$$

where \bar{h}_{iu}^{nm} represents the deterministic LoS component, and \hat{h}_{iu}^{nm} denotes the NLoS component. The Rician factor K influences the complex dynamics of the fading process.

B. Caching Model and Limited Transmit Power Budget

In order to minimize latency, increase data speed, and improve transmission efficiency, each UBD is provisioned with additional cache memory. This added memory facilitates the pre-loading of part of the data intended for transmission, thereby optimizing the overall data transfer process. In more

detail, each UBD retains a fraction of the data source within its cache. Let c_r represent the proportion of the data source stored by the caching model, where $0 \leq c_r \leq 1$, and let M denote the number of UBDs. When the destination requests a data source, a segment c_r of this file is already available in the storage of each UBD. Utilizing the caching mechanism, the BS transmits only a portion of the data source to the destination via the UBDs, with the transmitted amount being proportional to $(1 - c_r M_c)$, where M_c is the number of different cache coefficients c_r set in the UBDs. It is important to note that this caching model represents a lower bound for scenarios where the UAVs have prior knowledge of content popularity.

To optimize throughput at the destination while ensuring realistic power management, we impose separate constraints on the transmission power of the BS and UAV. This adjustment prevents the transmit powers from exceeding the respective hardware limitations of each device. The constraints are expressed for $\forall m \in \mathcal{M}, \forall n \in \mathcal{N}$ as follows

$$0 \leq P_s^{nm} \leq P_s^{\max}, 0 \leq P_u^{nm} \leq P_u^{\max}, \quad (6)$$

where P_s^{nm} and P_u^{nm} denote the transmit power of the BS and UBD, respectively, for UBD m at time slot n . Here, P_s^{\max} and P_u^{\max} represent the maximum allowable transmit power for the BS and UBD, respectively.

C. Energy Harvesting and Energy Consumption

Given the constrained power budget, it becomes imperative to consider EH to extend the operational lifespan of UBDs. To achieve this objective, a dynamic time-splitting mechanism is devised, which partitions each time slot into two phases for UBD communication. During a time slot of length δ_t , the UBD spends $\tau^{nm} \delta_t$ for transmission of backscattering signals and $(1 - \tau^{nm}) \delta_t$ for EH. The energy harvested by the UBD, denoted as E_h^{nm} , is computed as [37]

$$E_h^{nm} \triangleq \mu (1 - \tau^{nm}) \delta_t P_{WPT} \mathbb{E}\{|h_{su}^{nm}|^2\}, \quad (7)$$

where P_{WPT} represents the transmit power of the BS used during the EH phase, which lasts for $(1 - \tau^{nm}) \delta_t$ in the n -th time slot. The EH efficiency, denoted by μ , corresponds to the linear model of electromagnetic energy harvesters. The parameter τ^{nm} signifies dynamic time-division duplexing within each time slot. For instance, when $\tau^{nm} = 1$, the entire slot is allocated for backscattering signals to the destination. Conversely, when $\tau^{nm} = 0$, the entire slot is dedicated to EH. The expectation of the channel coefficient is given as

$$\mathbb{E}\{|h_{su}^{nm}|^2\} = \omega_0 / (d_{su}^{nm})^\alpha. \quad (8)$$

The classification of energy consumption for the UBDs involves three main energy components for backscattering, expended on propulsion, and for active communication with the destination. Specifically, the energy consumed by the m -th UBD for propulsion during the n -th time slot, denoted as

TABLE III
EXPERIMENTAL DATA

Parameters	Values
ρ	1.225 kg/m ³
I	0.1
A	0.8 m ²
δ	0.1
W	0.5 N
Ω	100 rad/s
R	0.08 m
s	0.05

E_{fly}^{nm} , is calculated using the rotary-wing model presented in [38] as

$$E_{fly}^{nm}(\mathbf{q}) = P_0 (\delta_t + \frac{k_1}{\delta_t} (\Delta^{nm})^2) + P_1 \sqrt{\sqrt{\delta_t^4 + k_2^2 (\Delta^{nm})^4} - k_2 (\Delta^{nm})^2} + \frac{k_3 (\Delta^{nm})^3}{\delta_t^2}, \quad (9)$$

where $P_0 = \frac{\delta}{8} \rho s A \Omega^3 R^3$, $P_1 = (1 + I) \frac{W^{3/2}}{\sqrt{2\rho A}}$, $k_1 = \frac{3}{\Omega^2 R^2}$, $k_2 = \frac{1}{2v_0^2}$, $k_3 = 0.5 d_0 \rho s A$. The model incorporates the profile drag coefficient δ , air density ρ [kg/m³], rotor solidity s , rotor disc area A [m²], blade angular velocity Ω [rad/s], rotor radius R [m], an incremental adaptation value I (set to 0.1) concerning the induced power, and UAV weight W [N] with specific values shown in Table III. During the n -th time slot, the model in (9) determines the energy consumed by the UAV's backscatter equipment, represented as $\tau^{nm} \delta_t P_b$, where P_b denotes the UAV's hardware power consumption during the backscatter phase [37]. An energy constraint for the UBD can be established, incorporating all the parameters mentioned

$$\sum_{i=1}^n (E_{fly}^{nm}(\mathbf{q}) + \tau^{nm} \delta_t (P_b + P_u^{nm})) \leq \sum_{i=1}^n E_h^{nm}. \quad (10)$$

This suggests that the total energy harvested by the UBD in the n -th time slot should exceed its cumulative energy consumption. By combining (7) to (10), a closed-form expression for the constraint in (10) can be derived:

$$\sum_{i=1}^n (E_{fly}^{nm}(\mathbf{q}) + \tau^{nm} \delta_t (P_b + P_u^{nm})) \leq \sum_{i=1}^n \frac{\mu (1 - \tau^{nm}) \delta_t \omega_0 P_{WPT}}{(d_{su}^{nm})^\alpha}. \quad (11)$$

D. Signal Model & Shannon Capacity

A time-division duplexing (TDD) protocol is employed, as extensively discussed in [26]. Each time slot is divided into two segments using the dynamic time splitting method: the intervals $(1 - \tau^{nm}) \delta_t$ and $\tau^{nm} \delta_t$ are respectively allocated for uplink data transmission from the BS to the UBD, and downlink data transmission from the UBD to the destination. The dynamic time splitting ratio for the n -th time slot adheres to the constraint $0 \leq \tau^{nm} \leq 1$. Denoting v_s^{nm} as the data symbol transmitted by the BS to the m -th UBD with unit power with $\mathbb{E}\{|v_s^{nm}|^2\} = 1$ during the n -th time slot, the received signal at m -th UBD can be expressed as

$$g_u^{nm} = \sqrt{P_s^{nm}} h_{su}^{nm} v_s^{nm} + n_u, \quad (12)$$

where $n_u \sim \mathcal{CN}(0, \sigma_u^2)$ represents the additive white Gaussian noise (AWGN) at the UBD. Furthermore, the signal v_u^{nm} , resulting from the backscattering by the m -th UBD during the n -th time slot, is given by [39] as

$$v_u^{nm} = \sqrt{\eta_u^n P_s^{nm}} h_{su}^{nm} v_s^{nm}, \quad (13)$$

whereas η_u^n , ranging from 0 to 1, denotes the backscatter coefficient for time slot n . Furthermore, the factors ignored in (13), such as supplementary noise and signal processing latency, are crucial and well documented in prior studies [37], [39], [40]. With the active link provided by the m -th UBD, the signal received at the destination is unfolded as

$$g_d^{nm} = h_{ud}^{nm} v_u^{nm} + \sqrt{P_u^{nm}} h_{ud}^{nm} v_s^{nm} + n_d. \quad (14)$$

where $n_d \sim \mathcal{CN}(0, \sigma_d^2)$ is the additive white Gaussian noise (AWGN) at the destination. The received signal at the destination due to backscattering and active data transmission from the BS and the m -th UBD during time slot n is denoted by $\sqrt{P_s^{nm}} h_{ud}^{nm} v_s^{nm}$ and $\sqrt{P_u^{nm}} h_{ud}^{nm} v_u^{nm}$, respectively. It is important to note that the noise power from backscattering, denoted as $\sqrt{\eta_u^n P_s^{nm}}$ in equation (14), is much lower than the baseband noise power [41] and is thus considered negligible in the equation's formulation. The overall received signal at the destination, integrating from (13) and (14), is

$$g_d^{nm} = \sqrt{\eta_u^n P_s^{nm}} h_{ud}^{nm} h_{su}^{nm} v_s^{nm} + [c_r] \sqrt{P_u^{nm}} h_{ud}^{nm} v_c^{nm} + n_d, \quad (15)$$

where v_c^{nm} represents the transmitted data symbol cached within the UBD m , with an expected power $\mathbb{E}\{|v_c^{nm}|^2\} = 1$. $[c_r]$ denotes the ceiling function of c_r . The term $\sqrt{P_u^{nm}} h_{ud}^{nm} v_c^{nm}$ indicates that if a c_r fraction of the requested file is cached within the UBD's storage, the UBD can then transmit the cached signal to the destination. Consequently, the signal-to-noise ratio (SNR) at the destination can be expressed as

$$\text{SNR}_d^{nm} = \frac{\eta_u^n P_s^{nm} |h_{ud}^{nm}|^2 |h_{su}^{nm}|^2 + P_u^{nm} [c_r] |h_{ud}^{nm}|^2}{\sigma_d^2}. \quad (16)$$

Here, the variance of noise power at the destination, n_d , is indicated by σ_d^2 in the equation. In the n -th time slot, the data throughput, measured in bps, at the UBD m and the destination can be respectively computed as follows:

$$R_u^{nm} = B \log_2(1 + \text{SNR}_u^{nm}), \quad (17)$$

$$R_d^{nm} = B \log_2(1 + \text{SNR}_d^{nm}), \quad (18)$$

where B (Hz) represents the system bandwidth and $\text{SNR}_u^{nm} = P_s^{nm} |h_{su}^{nm}|^2 / \sigma_u^2$. Notably, the instantaneous channel state information (CSI), including h_{su}^{nm} and h_{ud}^{nm} , is characterized as a random variable. Consequently, the instantaneous data throughput also exhibits the characteristics of a random variable. In light of this, we consider the approximated received data throughputs for the UBD and the destination, which can be formulated as follows:

$$\bar{R}_u^{nm} = B \mathbb{E}\{\log_2(1 + \text{SNR}_u^{nm})\}, \quad (19)$$

$$\bar{R}_d^{nm} = B \mathbb{E}\{\log_2(1 + \text{SNR}_d^{nm})\}. \quad (20)$$

Deriving a closed-form expression for \bar{R}_u^{nm} and \bar{R}_d^{nm} is a challenging task. Consequently, Lemma 1 provides the expressions for \bar{R}_u^{nm} and \bar{R}_d^{nm} through approximation functions.

Lemma 1. *Approximations for \bar{R}_u^{nm} and \bar{R}_d^{nm} can be formulated using closed-form expressions as follows:*

$$\bar{R}_u^{nm} = B \log_2 \left(1 + \frac{e^{-E} \omega_0 P_s^{nm}}{(d_{su}^{nm})^\alpha \sigma_u^2} \right), \quad (21)$$

$$\bar{R}_d^{nm} = B \log_2 \left(1 + \frac{\theta (\eta_u^n \omega_0 P_s^{nm} + \bar{P}_u^{nm} (d_{su}^{nm})^\alpha)}{\varrho} \right), \quad (22)$$

where $\theta \triangleq \frac{e^{-E} \omega_0}{\sigma_d^2}$, $\bar{P}_u^{nm} \triangleq P_u^{nm} [c_r]$, $\varrho \triangleq (d_{su}^{nm})^\alpha (d_{du}^{nm})^\alpha$.

Proof. Let us consider a function $f(x) = \mathbb{E}\{\log_2(1+x)\}$ with $x > 0$. Consequently, $f(x) = \mathbb{E}\{\log_2(1+e^{\ln x})\}$, $x > 0$. By applying Jensen's inequality to the convex function $\log_2(1+e^{\ln x})$ with respect to $\ln x$ variable, we get:

$$f(x) \geq \log_2(1+e^{\mathbb{E}\{\ln x\}}), \quad (23)$$

Denoting $x \triangleq P_s^{nm} |h_{su}^{nm}|^2 / \sigma_u^2$, x is an independent random variable following an exponential distribution with rate parameter $\lambda_f = (\mathbb{E}\{x\})^{-1} > 0$. Hence, $\lambda_f = (P_s^{nm} \omega_0 (d_{su}^{nm})^{-\alpha} / \sigma_u^2)^{-1}$. Using [[42], 4.331.1], we have

$$\begin{aligned} \mathbb{E}\{\ln x\} &= \int_0^{+\infty} \lambda_f e^{-\lambda_f x} \ln x dx = -(\ln \lambda_f + E) \\ &= \ln(P_s^{nm} \omega_0 (d_{su}^{nm})^{-\alpha} / \sigma_u^2) - E, \end{aligned} \quad (24)$$

where $E = 0.5772156649$ [[42], 4.331.1] is the Euler-Mascheroni constant. Thus, (21) is obtained by replacing (24) with (23). To prove (22), we consider $w(x, y) = \mathbb{E}\{\log_2(1+xy)\}$, $x > 0, y > 0$ with x, y being the independent random variables. By applying Jensen's inequality to the concave function $\log_2(1+xy)$ with respect to y variable, we get $w(x, y) \leq \log_2(1+x\mathbb{E}\{y\}) \triangleq \tilde{w}(x, y)$. Thus, $\tilde{w}(x, y) = \log_2(1+e^{\ln x} \mathbb{E}\{y\})$. Using Jensen's inequality for the convex function $\tilde{w}(x, y)$ and $\ln x$ variable, we obtain

$$\tilde{w}(x, y) \geq \log_2 \left(1 + e^{\ln \mathbb{E}\{x\}} \mathbb{E}\{y\} \right) \triangleq \hat{w}(x, y). \quad (25)$$

Since $\tilde{w}(x, y)$ can effectively approximate $w(x, y)$, although it does not serve as a definitive lower or upper bound. By applying [42, 4.331.1] and using the notations $x = |h_{ud}^{nm}|^2$, $y = (\eta_u^n P_s^{nm} |h_{su}^{nm}|^2 + P_u^{nm} [c_r]) / \sigma_d^2$, we then obtain

$$\begin{aligned} \mathbb{E}\{\ln x\} &= \int_0^{+\infty} \lambda_g e^{-\lambda_g x} \ln x dx = -(\ln \lambda_g + E) \\ &= \ln \left(\frac{\omega_0}{(d_{su}^{nm})^\alpha} \right) - E, \end{aligned} \quad (26)$$

$$\mathbb{E}\{y\} = (\eta_u^n P_s^{nm} \omega_0 (d_{su}^{nm})^{-\alpha} + \bar{P}_u^{nm}) / \sigma_d^2, \quad (27)$$

where $\lambda_g = (\mathbb{E}\{x\})^{-1} = (\omega_0 / (d_{su}^{nm})^\alpha)^{-1}$. The expression in equation (22) can be obtained by substituting (26) and (27) into (25). Consequently, Lemma 1 is conclusively proved. \square

E. Problem Formulation

The objective of this section is to develop a mathematical formulation aimed at maximizing the total data transmission from each UBD to the destination. This is achieved by jointly optimizing the DTS ratio, UBD trajectory and total transmit power under a linear EH mode. To formalize this optimization problem, we define $\mathbf{q} \triangleq \{\mathbf{q}^{nm}; n \in \mathcal{N}, m \in \mathcal{M}\}$,

$\boldsymbol{\tau} \triangleq \{\tau_n; n \in \mathcal{N}\}$, and $\mathbf{P} \triangleq \{P_u^n, P_s^n; n \in \mathcal{N}, m \in \mathcal{M}\}$. The problem is mathematically formulated as follows

$$\mathcal{P}_1 : \max_{\mathbf{q}, \boldsymbol{\tau}, \mathbf{P}} \sum_{m \in \mathcal{M}} \sum_{n \in \mathcal{N}} \tau^{nm} \delta_t \bar{R}_d^{nm}, \quad (28a)$$

$$\text{s.t.} \sum_{n \in \mathcal{N}} \tau^{nm} \delta_t \bar{R}_u^{nm} + c_r S \geq \sum_{n \in \mathcal{N}} \tau^{nm} \delta_t \bar{R}_d^{nm}, \forall m \in \mathcal{M}, \quad (28b)$$

$$\sum_{n \in \mathcal{N}} \tau^{nm} \delta_t \bar{R}_d^{nm} \geq S, \forall m \in \mathcal{M}, \quad (28c)$$

$$\begin{aligned} & \sum_{i=1}^n (E_{fly}^{nm}(\mathbf{q}) + \tau^{nm} \delta_t (P_b + P_u^{nm})) \\ & \leq \sum_{i=1}^n \frac{\mu(1 - \tau^{nm}) \delta_t w_0 P_{WPT}}{(d_{su}^{nm})^\alpha}, \forall m \in \mathcal{M}, \end{aligned} \quad (28d)$$

$$0 \leq P_s^{nm} \leq P_s^{\max}, \forall m \in \mathcal{M}, \forall n \in \mathcal{N}, \quad (28e)$$

$$0 \leq P_u^{nm} \leq P_u^{\max}, \forall m \in \mathcal{M}, \forall n \in \mathcal{N}, \quad (28f)$$

$$\|\mathbf{q}^{(n+1)m} - \mathbf{q}^{nm}\| \leq \delta_d = V_{\max} \delta_t, \forall m \in \mathcal{M}, \forall n \in \mathcal{N}, \quad (28g)$$

$$\mathbf{q}^{0m} = \mathbf{q}^{Im}, \quad \mathbf{q}^{nm} = \mathbf{q}^{Fm}, \forall m \in \mathcal{M}, \quad (28h)$$

$$0 \leq \tau^{nm} \leq 1, \forall n \in \mathcal{N}, \forall m \in \mathcal{M}. \quad (28i)$$

Here, S represents the data demanded by the destination. The constraint (28b) ensures that the data transmitted from the UBD must exceed the data received by the destination. The constraint (28c) stipulates that the total data transmitted on the downlink from a UBD must meet or exceed the destination's data requirements, ensuring adherence to user demands. The constraint (28d) mandates that the energy consumed by the UBD for flight, backscatter, and communication should not exceed its harvested energy. The constraint (28e) specifies that the maximum allowable power value should not be exceeded by the transmission energy of both the BS and the UBD.¹ Problem \mathcal{P}_1 is non-convex because its objective function and constraints (28b), (28c), (28d) are non-convex, making it hard to solve. Finding a solution for Problem \mathcal{P}_1 is nontrivial due to the inherent non-convexity.

Remark 1. *The rationale for considering a single destination is to focus on the core optimization aspects without introducing excessive complexity in channel modeling or data throughput evaluation. By limiting the setup to one end user, the characteristics of the wireless channels, backscatter reflection, and caching behavior can be carefully controlled and clearly analyzed. This setting allows us to validate the effectiveness of our proposed algorithm in a concise and well-isolated scenario. An extension to multi-user scenarios is conceptually straightforward but nontrivial with the presence of mutual interference as sharing time and frequency resources. Thus, each user is served by the multiple-UAV network, and the total throughput is of interest. Since the optimization structure and the underlying channel assumptions remain unchanged, the extension to N users would involve summing the individual*

¹One way to enhance the effectiveness of the transmission is to maximize the total data throughput since its inverse is proportional to the delay. The maximum tolerated delay for transmission depends on the specific requirements of network services, whereas the considered optimization framework maintains a generic form. Consequently, these constraints are potential for future work.

throughputs. This extension can be seamlessly incorporated into our formulation for future work.

III. BCD-BASED SOLUTION

To effectively address Problem \mathcal{P}_1 , we decompose it into three sub-problems. First, the DTS ratio is optimized with a fixed trajectory and initial power transmission. Then, the UBD trajectory is optimized, maintaining the DTS ratio fixed from the previous step and the same initial transmit power. Finally, the transmit power is optimized for given the DTS ratio and trajectory obtained in the preceding steps. By using the BCD [43], we design an iterative algorithm based on the KKT conditions.

A. Joint Trajectory and Dynamic Time Splitting Optimization

Given a trajectory \mathbf{q} and initial power transmission values \mathbf{P} for each UBD, the following optimization problem is formulated to obtain the DTS ratio $\boldsymbol{\tau}$

$$\mathcal{P}_1^\tau : \max_{\boldsymbol{\tau}} \sum_{m \in \mathcal{M}} \sum_{n \in \mathcal{N}} \tau^{nm} \delta_t \bar{R}_d^{nm} \quad (29a)$$

$$\text{s.t.} \sum_{n \in \mathcal{N}} \tau^{nm} \delta_t \bar{R}_u^{nm} + c_r S \geq \sum_{n \in \mathcal{N}} \tau^{nm} \delta_t \bar{R}_d^{nm}, \forall m \in \mathcal{M}, \quad (29b)$$

$$\sum_{n \in \mathcal{N}} \tau^{nm} \delta_t \bar{R}_d^{nm} \geq S, \forall m \in \mathcal{M}, \quad (29c)$$

$$\begin{aligned} & \sum_{i=1}^n (E_{fly}^{nm}(\mathbf{q}) + \tau^{nm} \delta_t (P_b + P_u^{nm})) \\ & \leq \sum_{i=1}^n \frac{\mu(1 - \tau^{nm}) \delta_t w_0 P_{WPT}}{(d_{su}^{nm})^\alpha}, \forall m \in \mathcal{M}, \end{aligned} \quad (29d)$$

$$0 \leq \tau^{nm} \leq 1, n \in \mathcal{N}, \forall m \in \mathcal{M}. \quad (29e)$$

Since the Slater's condition is satisfied by \mathcal{P}_1^τ , the KKT conditions are sufficient for optimality because Problem \mathcal{P}_1^τ is evidently a linear programming and therefore it is convex [44]. The Lagrangian function corresponding to problem \mathcal{P}_1^τ is expressed as follows

$$\begin{aligned} \mathcal{L}(\boldsymbol{\tau}, \lambda_1, \lambda_2, \lambda_3, \lambda_4) & \triangleq F(\boldsymbol{\tau}) + \lambda_1 G(\boldsymbol{\tau}) + \lambda_2 H(\boldsymbol{\tau}) + \lambda_3 I(\boldsymbol{\tau}) \\ & + \lambda_4 J(\boldsymbol{\tau}), \end{aligned} \quad (30)$$

where the following definitions hold

$$F(\boldsymbol{\tau}) \triangleq \sum_{n \in \mathcal{N}} \tau^{nm} \delta_t \bar{R}_d^{nm}, \quad (31)$$

$$G(\boldsymbol{\tau}) \triangleq \sum_{n \in \mathcal{N}} \tau^{nm} \delta_t \bar{R}_u^{nm} + c_r S - \sum_{n \in \mathcal{N}} \tau^{nm} \delta_t \bar{R}_d^{nm} \geq 0, \quad (32)$$

$$H(\boldsymbol{\tau}) \triangleq \sum_{n \in \mathcal{N}} \tau^{nm} \delta_t \bar{R}_d^{nm} - S \geq 0, \quad (33)$$

$$\begin{aligned} I(\boldsymbol{\tau}) & \triangleq \sum_{i=1}^n \frac{\mu(1 - \tau^{nm}) \delta_t w_0 P_{WPT}}{(d_{su}^{nm})^\alpha} \\ & - \sum_{i=1}^n (E_{fly}^{nm}(\mathbf{q}) + \tau^{nm} \delta_t (P_b + P_u^{nm})) \geq 0, \end{aligned} \quad (34)$$

$$J(\boldsymbol{\tau}) \triangleq 1 - \tau_n \geq 0, \quad (35)$$

where $\lambda_1, \lambda_2, \lambda_3, \lambda_4$ are Lagrangian dual variables.² Here, (32), (33), (34), and (35) are the primal feasibility conditions. Subsequently, the following expressions represent the complementary slackness conditions:

$$\lambda_1 G(\boldsymbol{\tau}) = 0, \lambda_2 H(\boldsymbol{\tau}) = 0, \lambda_3 I(\boldsymbol{\tau}) = 0, \lambda_4 J(\boldsymbol{\tau}) = 0, \quad (36)$$

with the given stationarity condition:

$$\begin{aligned} \frac{\partial L(\boldsymbol{\tau}, \lambda_1, \lambda_2, \lambda_3, \lambda_4)}{\partial \boldsymbol{\tau}} &= \sum_{n \in \mathcal{N}} \delta_t \bar{R}_d^{nm} + \\ \lambda_1 \left(\sum_{n \in \mathcal{N}} \delta_t \bar{R}_u^{nm} - \sum_{n \in \mathcal{N}} \delta_t \bar{R}_d^{nm} \right) &+ \lambda_2 \sum_{n \in \mathcal{N}} \delta_t \bar{R}_d^{nm} \\ - \lambda_3 \left(\sum_{n \in \mathcal{N}} X_1 + \sum_{n \in \mathcal{N}} \delta_t (P_b + P_u^{nm}) \right) &- \lambda_4 = 0, \end{aligned} \quad (37)$$

where $X_1 \triangleq (\mu \delta_t \omega_0 P_{\text{WPT}}) / (d_{su}^{nm})^\alpha$. For a feasible solution, the dual feasibility conditions should be satisfied with $\lambda_1, \lambda_2, \lambda_3, \lambda_4 \geq 0$. The solution that maximizes the objective function in \mathcal{P}_1^* is selected to achieve this optimal outcome. In the following theorem, two possible solutions for the optimal value of $\boldsymbol{\tau}$ are postulated.

Theorem 1. *The optimal value for problem \mathcal{P}_1^* , denoted as $\{\tau_n^{m*}\}$, $n \in \mathcal{N}, \forall m \in \mathcal{M}$, can be represented as follows:*

$$\tau^{nm*} = \frac{c_r S}{N \delta_t (\bar{R}_d^{nm} - \bar{R}_u^{nm})}, \text{ iff } \bar{R}_d^{nm} > \bar{R}_u^{nm}, \quad (38a)$$

$$\tau^{nm*} = \frac{X_1 - E_{\text{fly}}^{nm}(\mathbf{q})}{X_1 + \delta_t (P_b + P_u^{nm})}. \quad (38b)$$

Proof. If $J(\boldsymbol{\tau}) = 0$, it implies that $\tau^{nm} = 1$, which is not a suitable solution because it would not maintain both data transmission and energy harvesting. Therefore, we deduce $\lambda_4 = 0$. To find a feasible solution, we examine all possible cases as follows

Case 1: $\lambda_1 = 0, \lambda_2 = 0, \lambda_3 = 0$. According to (37), $\sum_{n \in \mathcal{N}} \delta_t \bar{R}_d^{nm} = 0$, which is not a reasonable outcome. Therefore, this case is not possible.

Case 2: $\lambda_1 = 0, H(\boldsymbol{\tau}) = 0, I(\boldsymbol{\tau}) = 0$. From $H(\boldsymbol{\tau}) = 0$, it follows that $\tau^{nm} = \frac{S}{N \delta_t \bar{R}_d^{nm}}$. Similarly, from $I(\boldsymbol{\tau}) = 0$, we find $\tau^{nm} = \frac{X_1 - E_{\text{fly}}^{nm}(\mathbf{q})}{X_1 + \delta_t (P_b + P_u^{nm})}$. This results in two different optimal values for τ , which is contradictory. Therefore, this case is not possible.

Case 3: $G(\boldsymbol{\tau}) = 0, \lambda_2 = 0, I(\boldsymbol{\tau}) = 0$.

Case 4: $G(\boldsymbol{\tau}) = 0, H(\boldsymbol{\tau}) = 0, \lambda_3 = 0$.

As Case 2, Case 3 and Case 4 also get two different values for τ , these cases are not possible.

Case 5: $G(\boldsymbol{\tau}) = 0, H(\boldsymbol{\tau}) = 0, I(\boldsymbol{\tau}) = 0$. In this case, we get up to three different τ values, which is absurd. As a result, this case is not possible.

²The optimal Lagrangian dual variables derived via the KKT conditions represent the *shadow prices* of the coupled network resources. Specifically, the dual variable associated with the energy-harvesting constraint strictly quantifies the marginal utility of power, representing the exact, infinitesimal increment in the total network throughput that would be achieved if the UAV is granted one additional Joule of harvested RF energy. Conversely, the dual variable enforcing the strict time-slot duration acts as a penalty for temporal violations, dictating the precise equilibrium trade-off between the energy-gathering and the active data-transmission phases.

Case 6: $G(\boldsymbol{\tau}) = 0, \lambda_2 = 0, \lambda_3 = 0$. From (37), we find $\lambda_1 = \frac{\sum_{n \in \mathcal{N}} \delta_t \bar{R}_d^{nm}}{\sum_{n \in \mathcal{N}} \delta_t \bar{R}_u^{nm} - \sum_{n \in \mathcal{N}} \delta_t \bar{R}_d^{nm}}$. If $\bar{R}_u^{nm} = \bar{R}_d^{nm}$, then $\lambda_1 = +\infty$. If $\bar{R}_u^{nm} > \bar{R}_d^{nm}$, then $\lambda_1 < 0$. Both scenarios are unreasonable. If $\bar{R}_u^{nm} < \bar{R}_d^{nm}$, then $\lambda_1 > 1$. Additionally, given $G(\boldsymbol{\tau}) = 0$, one has

$$\tau^{nm} = \frac{c_r S}{N \delta_t (\bar{R}_d^{nm} - \bar{R}_u^{nm})}. \quad (39)$$

According to (38), the optimal solution $\{\tau_n^{m*}\}$ can be determined when $\bar{R}_u^{nm} < \bar{R}_d^{nm}, \forall n \in \mathcal{N}, \forall m \in \mathcal{M}$.

Case 7: $\lambda_1 = 0, H(\boldsymbol{\tau}) = 0, \lambda_3 = 0$. From (37), $\lambda_2 = -1$ is not a reasonable outcome. Thus, this case is not possible.

Case 8: $\lambda_1 = 0, \lambda_2 = 0, I(\boldsymbol{\tau}) = 0$. From (37), we have

$$\lambda_3 = \frac{\sum_{n \in \mathcal{N}} \delta_t \bar{R}_d^{nm}}{\sum_{n \in \mathcal{N}} X_1 + \sum_{n \in \mathcal{N}} \delta_t (P_b + P_u^{nm})} \geq 0. \quad (40)$$

Additionally, for given $I(\boldsymbol{\tau}) = 0$, we have

$$\tau^{nm} = \frac{X_1 - E_{\text{fly}}^{nm}(\mathbf{q})}{X_1 + \delta_t (P_b + P_u^{nm})}. \quad (41)$$

We can derive (38) by combining (39), (41), and constraint (29a), completing the proof of Theorem 1. \square

The closed-form solution for τ_{nm}^* derived via the unconstrained KKT derivatives is physiologically valid only if it strictly resides within the interval $(0, 1)$. To ensure uninterrupted mathematical continuity, our algorithm implements a strict boundary safeguard: if the computed interior point violates the physical constraints $\tau_{nm}^* \notin (0, 1)$, the solution is set to the boundary that maximizes instantaneous EH, securing continuous constraint enforcement without algorithmic collapse. In which $E_{\text{fly}}^{nm}(\mathbf{q}), \bar{R}_u^{nm}, \bar{R}_d^{nm}, X_1$ are updated each time the loop calculates τ^{nm} . To attain the optimal result, the solution that yields the maximum value of the objective function of \mathcal{P}_1^* is selected. The feasibility ensures the optimal values obtained from (38a) and (38b) lie within their bounds.

B. Proceed With Trajectory Optimization

For given $\boldsymbol{\tau}$ and \mathbf{P} , UBDs's trajectories \mathbf{q} can be determined by solving the following problems:

$$\mathcal{P}_1^{\mathbf{q}} : \max_{\mathbf{q}} \sum_{m \in \mathcal{M}} \sum_{n \in \mathcal{N}} \tau^{nm} \delta_t \bar{R}_d^{nm} \quad (42a)$$

$$\text{s.t. } \sum_{n \in \mathcal{N}} \tau^{nm} \delta_t \bar{R}_u^{nm} + c_r S \geq \sum_{n \in \mathcal{N}} \tau^{nm} \delta_t \bar{R}_d^{nm}, \forall m \in \mathcal{M}, \quad (42b)$$

$$\sum_{n \in \mathcal{N}} \tau^{nm} \delta_t \bar{R}_d^{nm} \geq S, \forall m \in \mathcal{M}, \quad (42c)$$

$$\begin{aligned} \sum_{i=1}^n (E_{\text{fly}}^{nm}(\mathbf{q}) + \tau^{nm} \delta_t (P_b + P_u^{nm})) \\ \leq \sum_{i=1}^n \frac{\mu(1 - \tau^{nm}) \delta_t \omega_0 P_{\text{WPT}}}{(d_{su}^{nm})^\alpha}, \forall m \in \mathcal{M}, \end{aligned} \quad (42d)$$

$$\|\mathbf{q}^{(n+1)m} - \mathbf{q}^{nm}\| \leq \delta_d = V_{\max} \delta_t, \forall m \in \mathcal{M}, \forall n \in \mathcal{N}, \quad (42e)$$

$$\mathbf{q}^{0m} = \mathbf{q}^{Im}, \mathbf{q}^{nm} = \mathbf{q}^{Fm}, \forall m \in \mathcal{M}. \quad (42f)$$

The non-convexity of problem $\mathcal{P}_1^{\mathbf{q}}$ complicates solving it with standard optimization methods. To address this, the BCD is utilized. Introducing slack variables a^{nm} and b^{nm} , where

$\|\mathbf{q}^{nm} - \mathbf{W}_s\|^\alpha \leq a^{nm}$ and $\|\mathbf{q}^{nm} - \mathbf{W}_d\|^\alpha \leq b^{nm}$, enhances tractability. These variables, denoted as $\mathbf{z} \triangleq \{a^{nm}, b^{nm}, n \in \mathcal{N}\}$, allow Problem $\mathcal{P}_1^{\mathbf{q}}$ to be rewritten as

$$\mathcal{P}_{1.1}^{\mathbf{q}} : \max_{\mathbf{q}, \mathbf{z}} B \sum_{m \in \mathcal{M}} \sum_{n \in \mathcal{N}} \tau^{nm} \delta_t \log_2 \left(1 + \frac{\theta(\Theta + \bar{P}_u^{nm} a^{nm})}{a^{nm} b^{nm}} \right) \quad (43a)$$

$$\text{s.t. } \|\mathbf{q}^{nm} - \mathbf{W}_s\|^\alpha \leq a^{nm}, \forall m \in \mathcal{M}, \forall n \in \mathcal{N}, \quad (43b)$$

$$\|\mathbf{q}^{nm} - \mathbf{W}_d\|^\alpha \leq b^{nm}, \forall m \in \mathcal{M}, \forall n \in \mathcal{N}, \quad (43c)$$

$$B \sum_{n \in \mathcal{N}} \tau^{nm} \delta_t \log_2 \left(1 + \frac{e^{-E} \omega_0 P_s^{nm}}{a^{nm} \sigma_u^2} \right) + c_r S \\ \geq B \sum_{n \in \mathcal{N}} \tau^{nm} \delta_t \log_2 \left(1 + \frac{\theta(\eta_u^n \omega_0 P_s^{nm} + \bar{P}_u^{nm} a^{nm})}{a^{nm} b^{nm}} \right), \\ \forall m \in \mathcal{M}, \quad (43d)$$

$$B \sum_{n \in \mathcal{N}} \tau^{nm} \delta_t \log_2 \left(1 + \frac{\theta(\eta_u^n \omega_0 P_s^{nm} + \bar{P}_u^{nm} a^{nm})}{a^{nm} b^{nm}} \right) \\ \geq S, \forall m \in \mathcal{M}, \quad (43e)$$

$$\sum_{i=1}^n (E_{\text{fly}}^{nm}(\mathbf{q}) + \tau^{nm} \delta_t (P_b + P_u^{nm})) \\ \leq \sum_{i=1}^n \frac{\mu(1 - \tau^{nm}) \delta_t \omega_0 P_{WPT}}{a^{nm}}, \forall m \in \mathcal{M}, \quad (43f)$$

$$(42e), (42f), \quad (43g)$$

where $\Theta = \eta_u^n \omega_0 P_s^{nm}$. Because the problem remains challenging to solve, it is further handled by using the following established lemmas.

Lemma 2. For each a_j^{nm} and b_j^{nm} in the j -th-loop, applying the first-order Taylor approximation, one obtains

$$\log_2 \left(1 + \frac{e^{-E} \omega_0 P_s^{nm}}{a^{nm} \sigma_u^2} \right) \geq \log_2 \left(1 + \frac{e^{-E} \omega_0 P_s^{nm}}{a_j^{nm} \sigma_u^2} \right) \\ - \frac{e^{-E} \omega_0 P_s^{nm} (a^{nm} - a_j^{nm})}{a_j^{nm} (a_j^{nm} \sigma_u^2 + e^{-E} \omega_0 P_s^{nm}) \ln 2} \triangleq \Theta_1, \quad (44)$$

$$\log_2 \left(1 + \frac{\theta(\eta_u^n \omega_0 P_s^{nm} + \bar{P}_u^{nm} a^{nm})}{a^{nm} b^{nm}} \right) \\ \geq \log_2 \left(1 + \frac{\theta(\eta_u^n \omega_0 P_s^{nm} + \bar{P}_u^{nm} a_j^{nm})}{a_j^{nm} b_j^{nm}} \right) \\ - \frac{\theta \eta_u^n \omega_0 P_s^{nm} (a^{nm} - a_j^{nm})}{a_j^{nm} (\theta \eta_u^n \omega_0 P_s^{nm} + a_j^{nm} (\theta \bar{P}_u^{nm} + b_j^{nm})) \ln 2} \\ - \frac{\theta (\eta_u^n \omega_0 P_s^{nm} + \bar{P}_u^{nm} a_j^{nm}) (b^{nm} - b_j^{nm})}{b_j^{nm} (\theta \eta_u^n \omega_0 P_s^{nm} + a_j^{nm} (\theta \bar{P}_u^{nm} + b_j^{nm})) \ln 2} \triangleq \Theta_2. \quad (45)$$

Proof. At any given feasible points x_j and y_j , Taylor approximation is used to approximate these convex functions [27], $\log_2(1 + \frac{T_1}{x})$ and $\log_2(1 + \frac{T_2 + T_3 x}{xy})(x, y \geq 0)$ as

$$\log_2 \left(1 + \frac{T_1}{x} \right) \geq \log_2 \left(1 + \frac{T_1}{x^j} \right) \\ - \frac{T_1}{x^j (x^j + T_1) \ln 2} (x - x^j), \quad (46)$$

$$\log_2 \left(1 + \frac{T_2 + T_3 x}{xy} \right) \geq \log_2 \left(1 + \frac{T_2 + T_3 x^j}{x^j y^j} \right) \\ - \frac{T_2 (x - x^j)}{x^j (T_2 + x^j (T_3 + y^j)) \ln 2} - \frac{(T_2 + T_3 x^j) (y - y^j)}{y^j (T_2 + x^j (T_3 + y^j)) \ln 2}. \quad (47)$$

Applying $T_1 \triangleq e^{-E} \omega_0 P_s^{nm}$, $x \triangleq a^{nm}$, $y \triangleq b^{nm}$, $T_2 \triangleq \Theta \eta_u^n \omega_0 P_s^{nm}$ and $T_3 \triangleq \Theta \bar{P}_u^{nm}$, we have proved the lemma. \square

Lemma 3. The first-order Taylor approximation is applied to each a_j^{nm} in the j -th iteration, resulting in

$$\frac{1}{a^{nm}} \geq \frac{1}{a_j^{nm}} - \frac{1}{(a_j^{nm})^2} (a^{nm} - a_j^{nm}) \triangleq \tilde{a}^{nm}. \quad (48)$$

The formulation of $E_{\text{fly}}^{nm}(\mathbf{q})$ constrained in (11) makes the problem $\mathcal{P}_{1.1}^{\mathbf{q}}$ is still non-convex. To address this issue, a slack variable y^{nm} is introduced as

$$\sqrt{\delta_t^4 + k_2^2 (\Delta^{nm})^4} - k_2 (\Delta^{nm})^2 \leq (y^{nm})^2, \forall n \in \mathcal{N}. \quad (49)$$

This results in a constraint $\delta_t^4 / (y^{nm})^2 \leq (y^{nm})^2 + 2k_2 (\Delta^{nm})^2$, which is non-convex. Applying the first-order Taylor approximation, we get:

$$\frac{\delta_t^4}{(y^{nm})^2} \leq 2y_j^{nm} (y^{nm} - y_j^{nm}) - 2k_2 \|\mathbf{q}_j^{(n+1)m} - \mathbf{q}_j^{nm}\|^2 + \\ (y_j^{nm})^2 + 4k_2 (\mathbf{q}_j^{(n+1)m} - \mathbf{q}_j^{nm})^T (\mathbf{q}^{(n+1)m} - \mathbf{q}^{nm}), \forall n \in \mathcal{N}, \quad (50)$$

$E_{\text{fly}}^{nm}(\mathbf{q})$ can be replaced with its upper bound $\bar{E}_{\text{fly}}^{nm}(\mathbf{q})$ as

$$E_{\text{fly}}^{nm}(\mathbf{q}) \leq P_0 (\delta_t + k_1 (\Delta^{nm})^2) + P_1 y^{nm} + \frac{k_3 (\Delta^{nm})^3}{\delta_t^2} \\ \triangleq \bar{E}_{\text{fly}}^{nm}(\mathbf{q}). \quad (51)$$

By synthesizing Lemma 2, Lemma 3, and the previous manipulations, in the j -th iteration, the approximate convex problem is expressed as follows:

$$\mathcal{P}_{1.2}^{\mathbf{q}} : \max_{\mathbf{q}, \mathbf{z}} B \sum_{m \in \mathcal{M}} \sum_{n \in \mathcal{N}} \tau^{nm} \delta_t \Theta_2 \quad (52a)$$

$$\text{s.t. } (43e), (43f), (44b), (44c), \quad (52b)$$

$$B \sum_{n \in \mathcal{N}} \tau^{nm} \delta_t \Theta_1 + c_r S \geq B \sum_{n \in \mathcal{N}} \tau^{nm} \delta_t \Theta_2, \forall m \in \mathcal{M}, \quad (52c)$$

$$B \sum_{n \in \mathcal{N}} \tau^{nm} \delta_t \Theta_2 \geq S, \forall m \in \mathcal{M}, \quad (52d)$$

$$\frac{\delta_t^4}{(y^{nm})^2} \leq (y_j^{nm})^2 + 2y_j^{nm} (y^{nm} - y_j^{nm}) \\ - 2k_2 \|\mathbf{q}_j^{(n+1)m} - \mathbf{q}_j^{nm}\|^2 + 4k_2 (\mathbf{q}_j^{(n+1)m} - \mathbf{q}_j^{nm})^T \\ \times (\mathbf{q}^{(n+1)m} - \mathbf{q}^{nm}), \forall n \in \mathcal{N}, \forall m \in \mathcal{M}, \quad (52e)$$

$$\sum_{i=1}^n (\bar{E}_{\text{fly}}^{nm}(\mathbf{q}) + \tau^{nm} \delta_t (P_b + P_u^{nm})) \leq \\ \sum_{i=1}^n \mu(1 - \tau^{nm}) \delta_t \omega_0 P_{WPT} \tilde{a}^{nm} \forall m \in \mathcal{M}. \quad (52f)$$

Standard optimization methods can directly solve $\mathcal{P}_{1.2}^{\mathbf{q}}$ since the objective and all constraints are convex [44], [45].

C. Optimize The Total Transmit Power

The objective is recalculated with optimal variables P_s^{nm} , P_u^{nm} , adhering to these constraints:

$$\mathcal{P}_1^{\mathbf{P}} : \max_{\mathbf{P}} \sum_{m \in \mathcal{M}} \sum_{n \in \mathcal{N}} \tau^{nm} \delta_t \bar{R}_d^{nm}, \quad (53a)$$

$$\text{s.t. } \sum_{n \in \mathcal{N}} \tau^{nm} \delta_t \bar{R}_u^{nm} + c_r S \geq \sum_{n \in \mathcal{N}} \tau^{nm} \delta_t \bar{R}_d^{nm}, \forall m \in \mathcal{M}, \quad (53b)$$

$$\sum_{n \in \mathcal{N}} \tau^{nm} \delta_t \bar{R}_d^{nm} \geq S, \forall m \in \mathcal{M}, \quad (53c)$$

$$\sum_{i=1}^n (E_{\text{fly}}^{nm}(\mathbf{q}) + \tau^{nm} \delta_t (P_b + P_u^{nm})) \leq \sum_{i=1}^n \frac{\mu(1 - \tau^{nm}) \delta_t w_0 P_{\text{WPT}}}{(d_{su}^{nm})^\alpha}, \forall m \in \mathcal{M}, \quad (53d)$$

$$0 \leq P_s^{nm} \leq P_s^{\max}, \forall m \in \mathcal{M}, \forall n \in \mathcal{N}, \quad (53e)$$

$$0 \leq P_u^{nm} \leq P_u^{\max}, \forall m \in \mathcal{M}, \forall n \in \mathcal{N}. \quad (53f)$$

To simplify solving the optimization problem, we will transform the involved functions into convex functions with respect to the optimization variable. For ease of notation, we define $l_1^{nm} \triangleq \|\mathbf{q}^{nm} - \mathbf{W}_s\|^\alpha$ and $l_2^{nm} \triangleq \|\mathbf{q}^{nm} - \mathbf{W}_d\|^\alpha$.

Lemma 4. For each $P_{s,j}^{nm}$ and $P_{u,j}^{nm}$ in the j th-loop, applying the first-order Taylor approximation, we get:

$$\begin{aligned} & \log_2 \left(1 + \frac{\theta P_s^{nm}}{l_1^{nm}} \right) \cong \log_2 \left(1 + \frac{\theta P_{s,j}^{nm}}{l_1^{nm}} \right) \\ & + \frac{\theta(P_s^{nm} - P_{s,j}^{nm})}{(l_1^{nm} + \theta P_{s,j}^{nm}) \ln 2} \triangleq \tilde{\Theta}_1, \quad (54) \\ & \log_2 \left(1 + \frac{\theta(\eta_u^n \omega_0 P_s^{nm} + \bar{P}_u^{nm} l_1^{nm})}{l_1^{nm} l_2^{nm}} \right) \\ & \cong \log_2 \left(1 + \frac{\theta(\eta_u^n \omega_0 P_{s,j}^{nm} + \bar{P}_{u,j}^{nm} l_1^{nm})}{l_1^{nm} l_2^{nm}} \right) \\ & - \frac{\theta \eta_u^n \omega_0 (P_s^{nm} - P_{s,j}^{nm}) + \theta l_1^{nm} [c_r] (P_u^{nm} - P_{u,j}^{nm})}{(l_1^{nm} l_2^{nm} + \theta \eta_u^n \omega_0 P_{s,j}^{nm} + \theta l_1^{nm} [c_r] P_{u,j}^{nm}) \ln 2} \triangleq \tilde{\Theta}_2. \quad (55) \end{aligned}$$

Proof. At any given feasible points u_j and t_j , Taylor approximation is used to approximate these functions, $\log_2(1 + T_1 u)$ and $\log_2(1 + T_2 u + T_3 t)$ ($u, t \geq 0$), individually:

$$\log_2(1 + T_1 u) \cong \log_2(1 + T_1 u_j) + \frac{T_1}{(1 + T_1 u_j) \ln 2} (u - u_j), \quad (56)$$

$$\begin{aligned} & \log_2(1 + T_2 u + T_3 t) \cong \log_2(1 + T_2 u_j + T_3 t_j) \\ & + \frac{T_2(u - u_j) + T_3(t - t_j)}{(1 + T_2 u_j + T_3 t_j) \ln 2}. \quad (57) \end{aligned}$$

By applying $T_1 \triangleq \theta/l_1^{nm}$, $T_2 \triangleq \theta \eta_u^n \omega_0 / l_1^{nm} l_2^{nm}$, $T_3 \triangleq [c_r] \theta / l_2^{nm}$, $u \triangleq P_s^{nm}$, and $t \triangleq P_u^{nm}$, we have proved Lemma 4. \square

Applying Lemma 4, Problem $\mathcal{P}_1^{\mathbf{P}}$ is reformulated as

$$\mathcal{P}_{1.1}^{\mathbf{P}} : \max_{\mathbf{P}} B \sum_{m \in \mathcal{M}} \sum_{n \in \mathcal{N}} \tau^{nm} \delta_t \tilde{\Theta}_2 \quad (58a)$$

$$\text{s.t. } B \sum_{n \in \mathcal{N}} \tau^{nm} \delta_t \tilde{\Theta}_1 + c_r S \geq B \sum_{n \in \mathcal{N}} \tau^{nm} \delta_t \tilde{\Theta}_2, \forall m \in \mathcal{M}, \quad (58b)$$

$$B \sum_{n \in \mathcal{N}} \tau^{nm} \delta_t \tilde{\Theta}_2 \geq S, \forall m \in \mathcal{M}, \quad (58c)$$

$$\sum_{i=1}^n (E_{\text{fly}}^{nm}(\mathbf{q}) + \tau^{nm} \delta_t (P_b + P_u^{nm})) \leq \sum_{i=1}^n \frac{\mu(1 - \tau^{nm}) \delta_t w_0 P_{\text{WPT}}}{(d_{su}^{nm})^\alpha}, \forall m \in \mathcal{M}, \quad (58d)$$

$$0 \leq P_s^{nm} \leq P_s^{\max}, \forall m \in \mathcal{M}, \forall n \in \mathcal{N}, \quad (58e)$$

$$0 \leq P_u^{nm} \leq P_u^{\max}, \forall m \in \mathcal{M}, \forall n \in \mathcal{N}. \quad (58f)$$

Let the surrogate functions defined in the BCD serve as strict global lower bounds to the original non-convex constraints. Under the block-coordinate update rule, the objective value sequence generated by Algorithm 1 is monotonically non-decreasing. Since the maximum throughput is strictly upper-bounded by finite transmission power budgets and spectrum allocations, the sequence converges to a finite stationary point satisfying the KKT conditions. $\mathcal{P}_{1.1}^{\mathbf{P}}$ can be directly solved using standard optimization methods because the objective function and all constraints are convex [44], [45]. While the BCD mathematically guarantees convergence to a stationary point, it relies on replacing the expected value of a non-convex rate function with a deterministic lower bound. Specifically, estimating the expected achievable data rate over probabilistic fading channels by substituting the instantaneous channel gain with its mean introduces a systematic overestimation due to Jensen's Inequality, mathematically defined as $\mathbb{E}[\log_2(1 + X)] \leq \log_2(1 + \mathbb{E}[X])$. By evaluating a second-order Taylor series expansion of the logarithmic rate function, this approximation error is proportional to the variance of the channel fading distribution. Consequently, these Taylor expansions remain exceptionally tight and theoretically sound in static topologies or high-SNR, LoS-dominant regimes where variance is suppressed. Under low-SNR conditions or in rapidly varying channels with high Doppler spreads and extreme UAV mobility, the variance increases drastically. In such hostile environments, the BCD bounds loosen severely, which may lead the deterministic solver to converge upon a mathematically valid but physically sub-optimal trajectory.

The convergence of the BCD to a stationary point is theoretically guaranteed by satisfying three fundamental groups of conditions. Firstly, regarding the feasible sets, the multi-variable optimization space is fully decoupled into independent, convex, and closed constraint blocks (i.e., dynamic time splitting, UAV trajectory, and transmit power). Secondly, the original non-convex objective function (total system throughput) is continuous, possesses block-wise Lipschitz continuous gradients, and is fundamentally upper-bounded by the finite WPT energy budget and physical channel capacities. Thirdly, and most critically, the surrogate functions constructed

Algorithm 1 Solve Problem \mathcal{P}_1 using the BCD

Require: Set $j = 0$, $i = 0$ and initial values for \mathbf{q}^i , τ^i , \mathbf{P}^j .

- 1: **repeat**
- 2: **repeat**
- 3: For a given \mathbf{q}^i and \mathbf{P}^j , the problem \mathcal{P}_1^τ is solved, and the optimal solution is denoted as τ^* .
- 4: For a given τ^{i+1} and \mathbf{P}^j , the problem \mathcal{P}_1^q is solved, and the optimal solution is denoted as \mathbf{q}^* .
- 5: Update the local point $\tau^{i+1} = \tau^*$ and $\mathbf{q}^{i+1} = \mathbf{q}^*$.
- 6: Set $i \leftarrow i + 1$.
- 7: **until** Convergence with $\epsilon > 0$.
- 8: For a given \mathbf{q}^* and τ^* , the problem \mathcal{P}_1^P is solved, and the optimal solution is denoted as \mathbf{P}^* .
- 9: Update the local point $\mathbf{P}^{j+1} = \mathbf{P}^*$.
- 10: Set $j \leftarrow j + 1$.
- 11: **until** Convergence with $\epsilon > 0$.

via first-order Taylor expansions during the SCA procedure rigorously adhere to the following rules at any given local iteration point in the j -th loop: *Value Matching* (the surrogate equals the original function value at the local point, *Gradient Matching* (the first-order derivatives are identical, ensuring a valid ascent direction), and *Global Lower Bound* (the surrogate acts as a tight concave lower bound for the original non-convex maximization objective across the feasible set). By strictly satisfying these mathematical conditions, the algorithm yields a monotonically non-decreasing sequence of total throughput that is mathematically guaranteed to converge to a stable stationary point.

D. Complexity Analysis

The proposed closed-form expressions efficiently address Problem \mathcal{P}_1^τ , thereby resolving \mathcal{P}_1^q and \mathcal{P}_1^P as the primary subproblems in this context. Given that \mathcal{P}_1^q exhibits a logarithmic structure, its complexity is determined as $\mathcal{O}(L_1(3N)^{3.5})$, where L_1 is the number of iterations required to update the UBD trajectory, and $3N$ denotes the number of scalar variables involved [46]. Therefore, the overall computational complexity of \mathcal{P}_1^q and \mathcal{P}_1^τ is $\mathcal{O}(L_2L_1(3N)^{3.5})$, where L_2 is the number of iterations needed for convergence to be achieved. Similarly, the complexity associated with solving \mathcal{P}_1^q and \mathcal{P}_1^P is $\mathcal{O}(L_3(3N)^{3.5})$, where L_3 represents the iterations required to update the transmit power and $3N$ corresponds to the number of scalar variables. Thus, the total complexity of Algorithm 1 amounts to $\mathcal{O}(L_4(3N)^{3.5}(L_1L_2 + L_3))$, where L_4 is the number of iterations essential for convergence.³

IV. GA-BASED SOLUTION

We present the GA to solve Problem \mathcal{P}_1 , which begins by initializing a population of individuals and maintaining it

³The mathematical problem formulation assumes a fixed number of UAVs to maintain resource block allocations and ensure the feasibility of the collision-avoidance constraints. If scenarios involve a dynamic number of UAVs across multiple time slots, the centralized controller must adapt to the changing topology by either halting and re-triggering the optimization solver for a new network configuration with an updated number of UAVs.

throughout the search process. In each generation, a pair of individuals undergoes the crossover to create two new offspring subjected to the mutation. These offspring are evaluated and selected for the next generation based on their fitness.

Solution representation: The variables of the problem are the coordinates in 3D space $(x, y, z)^{nm}$, τ^{nm} , P_u^{nm} , P_s^{nm} . Here, q^{nm} represents the position of a UBD at time slot n , and its position is defined by the coordinates $(x, y, z)^{nm}$. We have $N = T/\delta_t$ time slots, and in of these time slots, the values of $(x, y, z)^{nm}$, τ^{nm} , P_u^{nm} , and P_s^{nm} vary. Therefore, each UBD is a population \mathcal{Q} consisting of \mathbf{I} individuals, where each individual is a $6 \times N$ -dimensional vector $c = \{c_1, c_2, \dots, c_{6 \times N}\}$ of real numbers in the range $(0, 1)$, representing the parameters of the problem at each time slot. To translate these values into real-world parameters, we multiply them by specific scaling factors chosen during the algorithm setup. Specifically,

- 1) Representing the coordinates $(x, y, z)^{nm}$ at the n -th time slots into the actual coordinates we get $x^{nm} = \{c_1, c_2, \dots, c_N\} \times X$, $y^{nm} = \{c_{N+1}, c_{N+2}, \dots, c_{2N}\} \times Y$, $z^{nm} = \{c_{2N+1}, c_{2N+2}, \dots, c_{3N}\} \times Z$, where X, Y, Z are the limit values of (x, y, z) coordinates in 3D space.
- 2) We set $\tau^{nm} = \{c_{3N+1}, c_{3N+2}, \dots, c_{4N}\} \times t$, $P_u^{nm} = \{c_{4N+1}, c_{4N+2}, \dots, c_{5N}\} \times P_U$, $P_s^{nm} = \{c_{5N+1}, c_{5N+2}, \dots, c_{6N}\} \times P_S$, where t, P_U and P_S are the limit values for τ^{nm} , P_u^{nm} and P_s^{nm} .

Fitness function: Before initializing the population, we define the fitness function $\text{Fitness}(c)_m$ of the m -th UBD as

$$\text{Fitness}(c)_m = \max \sum_{n=1}^N \tau^{nm} \log_2 \left(1 + \frac{\theta(n_u w_0 P_s^{nm} + \bar{P}_u^{nm} d_{su}^{nm})}{(d_{su}^{nm})^\alpha (d_{du}^{nm})^\alpha} \right). \quad (59)$$

Each individual within the population is assessed using the fitness function to determine its suitability. Individuals with higher fitness values are more likely to be selected for the next generation. According to the problem's objective, the function evaluates the solution to \mathcal{P}_1 . However, for a feasible individual in the population, it must satisfy the following constraints

- 1) The distance the UBD travels between two consecutive the n -th and $n + 1$ -th time slots must be less than the maximum distance the UBD can fly, as defined by (28g) and (28h).
- 2) The total flying energy of the UBD E_{fly}^{nm} must be less than the total energy harvested, E_h^{nm} , as in (28d).
- 3) The data transmission rate received at the destination must exceed the transmission rate of the UBD in (28b).
- 4) Finally, the data rate at the destination must be greater than the minimum rate S , to ensure technical requirements and user needs (28c).

If an individual c cannot satisfy the first three constraints, $\text{Fitness}(c)_m = 0$. However, if it meets the first three constraints but fails the last one, the fitness value of this individual will be penalized with a penalty factor according to the requirements

$$\text{Fitness}(c)_m \leftarrow p \times \text{Fitness}(c)_m, \quad (60)$$

where p is a penalty factor in the range of $(0, 1)$. To enforce the constraints (28e) and (28f), we restrict the values of P_u^{nm}

and P_s^{nm} from the outset of the algorithm. As explained, P_u^n and P_s^n for the n -th time slot are expressed as real numbers within the range of $(0, 1)$. Accordingly, we establish the initial constraints for P_u^{nm} , P_s^{nm} based on the specified P_{\max} . Nevertheless, due to the UBD's limitation, P_u^{nm} cannot exceed P_s^{nm} , necessitating an additional restriction on P_u^{nm} . To clarify, in this context,

$$P_u^{nm} = \{c_{4N+1}, c_{4N+2}, \dots, c_{5N}\} \times P_U, P_U \leq P_U^*, \quad (61)$$

$$P_s^{nm} = \{c_{5N+1}, c_{5N+2}, \dots, c_{6N}\} \times P_S. \quad (62)$$

Here, P_U and P_S serve as the limit values to satisfy the aforementioned constraint. Additionally, P_U^* is the upper bound imposed to restrict the value of P_U .

A. Population Initialization

In the population initialization, each individual is represented by a gene that signifies a potential solution. The population size is predefined and significantly impacts the performance of the GA. The diversity of the population is crucial to ensure the algorithm explores the entire solution space and avoids local optima. During initialization, each randomly generated individual is evaluated using the fitness function. Specifically, if $\text{Fitness}(c_i)_m > 0, \forall i \in \{0, \dots, I\}$, then c_i is added to the population. Otherwise, the candidate is eliminated. To enhance the efficiency of creating suitable individuals, we incorporate initial constraints (11) and (28g) into the initialization process.

Crossover: It is the process of combining two individuals (parents) to generate one or more offspring. This process mimics natural reproduction, in which genes from both parents are combined to produce offspring with genetic traits from both parents. The crossover introduces diversity into the population and aids in exploring new solutions. After initializing the initial population, the process of creating a new generation begins. First, we randomly select two individuals from the current population to serve as the parent individuals for the crossover process. We utilize crossover for binary arrays, specifically one-point crossover, to combine two parent individuals, f_a and m_o , to create two offspring c_1 and c_2 as $c_1 = u f_a + (1 - u) m_o, c_2 = (1 - u) f_a + u m_o$, where u is a real number in the range $(0, 1)$ representing the crossover point. This process is repeated $I/2$ times to generate a sub-population Q' consisting of individuals, with the total number of individuals in Q' equal to I .

Mutation: A random alteration of one or more genes is involved within an individual. This process simulates natural mutations, facilitating the creation of new traits and maintaining genetic diversity within the population. After the crossover, a population Q' is obtained. With the number of mutated individuals denoted as I_1 , the individuals in population Q' undergo mutation via replacement mutation process as follows: $I_1 = I\theta$, where θ is the mutation coefficient. These individuals are mutated by selecting any position and replacing it with a random number in the range $[0, 1)$.

Selection: Following the creation of offspring through the crossover and the mutation, these individuals are evaluated and selected to form the next generation. After the mutation, we

Algorithm 2 Solve Problem \mathcal{P}_1 using GA for UBDs.

- 1: Start by randomly initializing the initial population, denoted as Q and I individuals.
 - 2: Evaluate the fitness of each individual in the population using the predefined fitness function $\text{Fitness}(c)$.
 - 3: Set the maximum number of generations G_{\max} and initialize $G \leftarrow 0$.
 - 4: **for** $G \leftarrow 0$ to G_{\max} **do**
 - 5: Select parents from the initial population, Q .
 - 6: Perform crossover to create a new population, Q' .
 - 7: Apply mutation to the individuals in population Q' .
 - 8: Combine population Q' with the initial population Q , forming Q'' . Calculate the fitness of the individuals in Q'' , arranging them in descending order.
 - 9: Select 50% of the individuals from population Q'' to create a new population for the next iteration.
 - 10: **end for**
-

merge the population Q' with Q to create a population Q'' consisting of $2I$ individuals. According to the design, only I individuals are retained in the population. We rely on the fitness function to sort the individuals of Q'' in descending order. Then we employ hierarchical selection based on the fitness function to retain half the individuals. Specifically, we select 40% I of the best individuals, 40% I of the average individuals, and 20% I of the worst individuals. An overview of this evolutionary algorithm is presented in Algorithm 2.

Complexity Analysis: Algorithm 2 has the computational complexity depending on the genetic operators, the representation of the individuals, the population, and the fitness function. In total, the computational complexity is in the order of $\mathcal{O}(6NPG_{\max})$, where G_{\max} is the number of generations, P is the population size, and $6N$ is the size of the individuals.

V. NUMERICAL RESULTS

This section presents numerical results validating the performance of the proposed frameworks. All simulations are performed on a personal computer equipped with an AMD Ryzen 7 4800H CPU (2.9 GHz) and 16 GB RAM using MATLAB, noting that the BCD gets the support of the general-purpose CVX toolbox [47].⁴ The BS and destination are located at $\mathbf{W}_s = [5, 0, 0]^T$ and $\mathbf{W}_d = [15, 0, 0]^T$. To improve readability and ease intuitive understanding of the collected data, this analysis is limited to two UBDs. The initial and final points of the UAV₁ are denoted by $\mathbf{q}_1^1 = [0, 10, 10]^T$ and $\mathbf{q}_1^2 = [20, 10, 10]^T$, respectively. For UAV₂, $\mathbf{q}_2^1 = [0, 10, 5]^T$ and $\mathbf{q}_2^2 = [20, 10, 5]^T$ designate its initial and final points, respectively. The value of c_r is 0.35. The initial transmit power of the BS and the UBD are $P_s = 16$ dBm and $P_u = 5$ mW, respectively. Furthermore, a power level of $P_{\text{WPT}} \in [27, 40]$ dB [48] is designated for the BS during WPT. The other system parameters are shown in Table IV. The efficacy of the proposed algorithms is evaluated against

⁴In practical systems, the core network with the high computing capacity and parallel processing is expected to reduce the time consumption in the orders of magnitude in response to real-time resource allocation.

TABLE IV
SIMULATION PARAMETERS

Parameters	Values/Sweep Range
Maximum speed of UB, V_{max}	$20 \frac{m}{s}$
Power noise, σ^2	-90 dB
Path loss exponent, α	2.3
Total flight time of the UB, T	50 s
Backscatter power, P_b	$1 \mu W$
System bandwidth, B	1 MHz
channel power gain at reference distance, ω_o	-30 dB
Duration of one time slot, δ_t	0.5 s
EH coefficient, μ	0.84
Backscatter coefficient, η	0.5
Data demanded, S	50 Mbits
Maximum allowable total transmit power, P_{max}	60 mW
Optimization threshold, ϵ	10^{-4}
BS Coordinate, W_s	[5, 0, 0]
Destination (IoT Sink) Coordinate, W_d	[15, 0, 0]
UAV ₁ Initial/Final Coordinates, $\mathbf{q}_I^1/\mathbf{q}_F^1$	[0, 10, 10]/[20, 10, 10]
UAV ₂ Initial/Final Coordinates, $\mathbf{q}_I^2/\mathbf{q}_F^2$	[0, 10, 5]/[20, 10, 5]
WPT, P_{WPT}	40 dB (27 to 40 dB)
Time horizon / Slot duration, T / δ_t	60s/0.5s (20 to 60s)
Redundant caching ratio, c_r	0.45 (0.1 to 0.9)

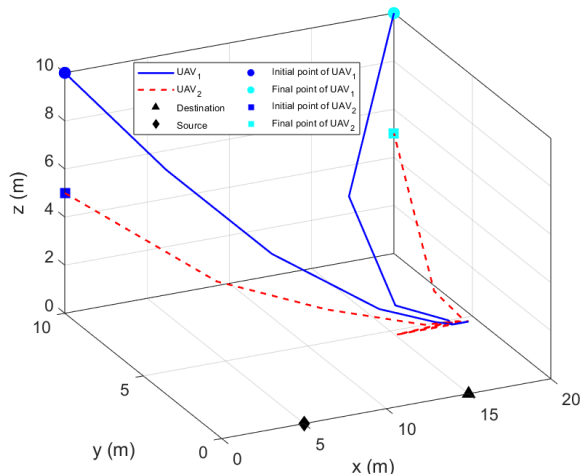


Fig. 3. The optimized trajectory of the two UAVs.

various benchmark schemes, which are detailed as follows: *i*) Complete (Com) represents the average throughput of fully implemented algorithms; *ii*) 3D+OP represents the average throughput of the algorithms, but with only one UBD; *iii*) 2D+2UAV uses the same algorithms as Com but does not optimize the transmit power and fix the flight trajectory height of the UBDs at height H .

Fig. 3 illustrates the trajectories of UAV₁ and UAV₂ derived using Algorithm 1. The UBD trajectories are designed to maintain a minimum altitude of three meters, ensuring compliance with safe operational parameters for UAVs in diverse environments. Each UBD commences at an initial point, transitions to a position near the line connecting the BS and destination, and concludes at its designated final point. During this movement, the UBDs typically descend to the lowest allowable altitude and follow a trajectory around a strategically chosen location situated on the direct line between the source and the destination. This strategy minimizes the distances between the devices, thereby enhancing both energy

collection and data transmission efficiency. Notably, the location around which the UBDs orbit is influenced by P_{WPT} [27], which dynamically adjusts the UBDs' paths to improve energy transfer and maximize the overall throughput.

Fig. 4(a) examines the relationship between the required data size and the overall throughput. The simulations conducted with $T = 30$ seconds, $P_{WPT} = 40$ dB, $V_{max} = 20$ m/s, $P_s = 15$ mW, $P_{max} = 20$ mW, and an initial reflection time $\tau = 0.4$. For Algorithm 1, the reflection time ratio c_r is 0.45, whereas for the 3D+OP approach, it is 0.9. The 2D+2UAV scenario employs a constant altitude of $H = 5$ meters for all the trajectories. Algorithm 1 obtains a significantly higher throughput than the others. Specifically, with a data demand of $S = 70$ Mbits, the throughput reaches 324.75 Mbits, compared to 210.24 Mbits and 316.12 Mbits for the 3D+OP and 2D+2UAV methods, respectively. These gains are attributed to the efficient utilization of all the available resources. Fig. 4(b) the throughput vs. P_{WPT} with $S = 20$ Mbits and the other settings keep the same as before. The proposed Com consistently obtains the highest throughput across all tested power levels. For instance, when $P_{WPT} = 30$ dB, the throughput values for the Com, 2D+2UAV, and 3D+OP strategies are 162.29 Mbits, 157.2 Mbits, and 136.12 Mbits, respectively. These findings emphasize that the proposed method can effectively optimize energy utilization. Fig. 4(c) delves into the impact of total travel time on performance metrics, with $P_{WPT} = 40$ dB, $S = 70$ Mbits, $\delta_t = 0.5$ s and $P_{max} = 60$ mW. We set c_r for each related benchmark as before. The altitude of the UBDs is fixed at $H = 10$ m in the 2D+2UAV method. All the benchmarks exhibit an increasing trend in total throughput as the travel time T increases. This is consistent with (28a), which predicts the total throughput at the destination scaling proportionally with the reflection time. The proposed algorithm significantly outperforms the benchmarks in overall throughput, demonstrating the effectiveness of our approach over benchmarks that do not utilize multiple UBDs or optimize total transmit power.

Under the constraints $V_{max} = 20$ m/s, $P_s = 16$ dBm, $S = 70$ Mbits, and $P_{max} = 60$ mW, the GA initializes a population of 100 individuals, a mutation rate of 0.1, and up to 10,000 generations. Along with the parameters above and under the constraints of Deep Reinforcement Learning (DRL), the Deep Deterministic Policy Gradient (DDPG) algorithm optimizes the UBD trajectory and communication performance. The DDPG agent is trained over 2000 episodes with a state dimension of 14 and an action dimension of 12. The Actor and Critic networks are updated using learning rates of 10^{-4} and 10^{-3} , respectively, with a batch size of 64. This configuration ensures efficient learning in continuous action spaces while adhering to the physical constraints of the UBD communication environment [49], [30]. Fig. 5(a) presents a comparative analysis of total throughput based on total movement time. The GA demonstrates a consistent advantage, achieving marginally higher throughput than the BCD. For instance, with movement times of 40 and 60 seconds, the GA yields throughputs of 508.36 Mbits and 727.85 Mbits, respectively, representing increases in DRL of 7.9% and 65%, respectively, under the same conditions. Meanwhile, the DRL

TABLE V
TOTAL THROUGHPUT AND COMPUTATIONAL TIME AMONG THE DRL, THE BCD, AND THE GA FOR VARIOUS VALUES OF WINDOW TIME

T	DRL			BCD			GA		
	Throughput	Training time	Inference time	Throughput	Running time	Iterations	Throughput	Running time	Generations
20	87.22 Mbits	2640 s	1.13 s	265.51 Mbits	569.51 s	15	295.88 Mbits	1168 s	9300
30	131.27 Mbits	3840 s	1.17 s	358.1 Mbits	1049.22 s	17	399.22 Mbits	2033 s	9600
40	175.33 Mbits	5280 s	1.24 s	466.52 Mbits	1453.8 s	20	508.36 Mbits	2940 s	10200
50	219.39 Mbits	6487 s	1.28 s	573.55 Mbits	2436.26 s	22	618.4 Mbits	3540 s	10600

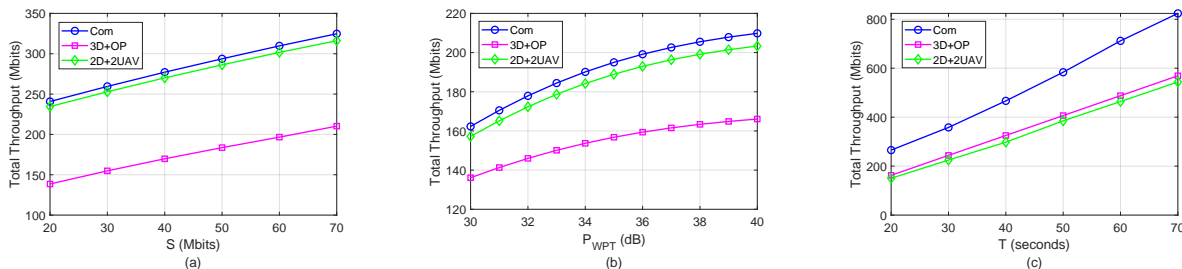


Fig. 4. Throughput comparison of scenarios with different parameter settings: (a) The total throughput versus the demanded data. (b) The total throughput versus P_{WPT} . (c) The total throughput versus traveling time T .

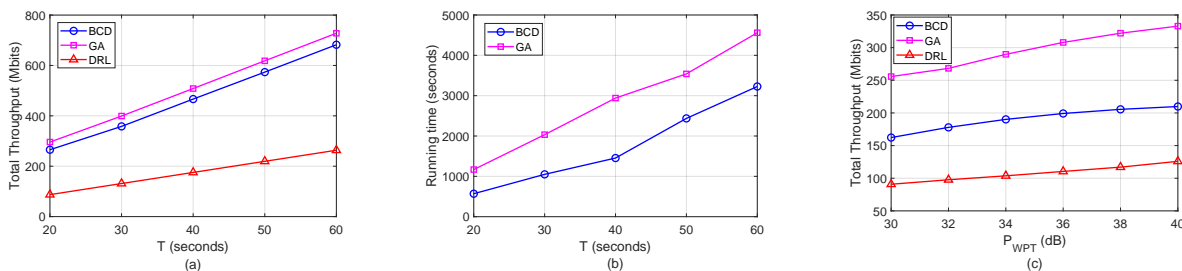


Fig. 5. Performance comparison between algorithms: (a) The total throughput versus the traveling time T . (b) The running time versus the traveling time T . (c) The total throughput versus the power transfer P_{WPT} .

approach exhibits significantly lower throughput performance due to its sensitivity to highly dynamic environments. These outcomes underscore the potential of the GA to effectively optimize throughput through evolutionary computation, albeit at a higher computational cost. Fig. 5(b) shows the total running time increasing significantly with the increase in the flight time T . Specifically, the time consumption of the GA is considerably higher than that of the BCD. As T is 50 seconds, the GA takes 31.19% longer than the BCD. This is because the computational complexity of the BCD mainly depends on trajectory and transmit-power optimization, as closed-form expressions for the optimal DTS values can be obtained. In contrast, the GA calculates the fitness for a large number of individuals in each iteration. Fig. 5(c) illustrates the variation in the total throughput with respect to the wireless power transfer parameter P_{WPT} . As P_{WPT} increases, all benchmarks exhibit gradual throughput improvements due to increased energy availability. Among them, the GA consistently achieves superior performance, maintaining an average gain of approximately 25% over the BCD and exceeding the DRL by more than 60%. For instance, when $P_{WPT} = 36$ dB, the GA attains about 308 Mbits, compared to 199 Mbits for BCD and 110 Mbits for DRL, representing improvements of roughly 54.7% and 180%, respectively. These findings reaffirm the robustness of the GA in optimizing the throughput across

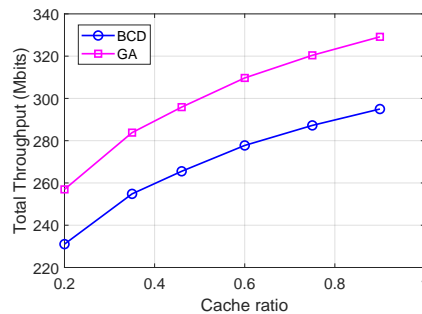


Fig. 6. The total throughput versus the cache ratio c_r .

varying transmission power levels.

Fig. 6 delves into the impact of the cache ratio c_r on the system performance, with $P_{WPT} = 40$ dB, $S = 70$ Mbits, $\delta_t = 0.5$ s, $P_{\max} = 60$ mW, and $T = 20$ seconds. In the low cache-ratio regime, e.g., transitioning from 0.2 to 0.3, the network demonstrates high responsiveness by mitigating the backhaul bottleneck, yielding significant throughput surges of approximately 17 Mbits for the BCD and 19 Mbits for the GA. However, as c_r approaches the extreme upper threshold, e.g., from 0.8 to 0.9, the marginal gain rapidly diminishes to roughly 5.1 Mbits and 5.8 Mbits for the BCD and the GA, respectively. The throughput and the computational cost comprising the training time and inference time are shown in Table V. From a performance perspective, the GA establishes

TABLE VI
COMPARING THE RUNNING TIME WITH/WITHOUT GPU

T(s)	20	30	40
BCD without GPU	569.52 s	1049.22 s	1454.8 s
BCD with GPU	7.47 s	13.35 s	18.26 s
GA without GPU	1168 s	2033 s	2940 s
GA with GPU	16 s	25 s	38 s

TABLE VII
COMPARING THE RUNNING TIME WITH GPU VS. THE NUMBER OF UAVS

Number of UAVs	2	4	6	7	10
BCD with GPU	7.47 s	25.84 s	58.12 s	79.45 s	168.32 s
GA with GPU	16.00 s	22.40 s	29.50 s	33.10 s	45.80 s

the upper bound for total network throughput, scaling from 295.88 Mb/s at $T = 20$ seconds to 618.40 Mb/s at $T = 50$ seconds, thereby outperforming the BCD and exceeding the DRL. However, this superiority of the GA comes at an expense of the computational cost. In contrast, the BCD demonstrates a highly efficient balance between optimality and complexity and presents a lighter computational burden than the GA while maintaining highly competitive throughput. Furthermore, the DRL exhibits a distinct two-stage execution paradigm. Although its offline training phase is computationally intensive, its online inference time is exceptionally brief.

All simulations have been executed on a personal computer with a central processing unit (CPU) only. To evaluate the algorithm's capability for near-real-time performance under practical deployment conditions, the algorithm is also implemented with GPU support using CUDA and tested on a workstation equipped with an NVIDIA RTX 4090 GPU. Comparative results are presented in Table VI. The dramatic runtime reductions reported were achieved by rewriting the mathematical objective functions into vectorized operations. For the BCD, the heavy matrix inversions required during the interior-point constraint evaluations were mapped to highly parallelized CUDA tensors. For the GA, the primary computational bottleneck, which is the fitness evaluation of thousands of complex 3D candidate trajectories, is parallelized, allowing the GPU to compute the fitness of the entire population simultaneously via batch matrix multiplications. The BCD is precise and efficient, leveraging solvers like CVX for convex problems, but it is limited by its inability to adapt to non-convex or dynamic environments. The GA is highly flexible and capable of global search, making it suitable for non-convex problems, though it is computationally expensive. The DRL has a long training time and high sample complexity, which remain significant challenges.

Table VII illustrates the offline running times of the BCD and GA algorithms with GPU acceleration [50] as the number of UAVs varies from two to ten. A critical crossover point in algorithmic efficiency is clearly observed as the network expands. For a minimal deployment of two UAVs, the deterministic BCD algorithm exhibits superior speed. However, as the number of UAVs increases, the computational burden of the BCD escalates sharply. In contrast, the GA demonstrates remarkable scalability under GPU acceleration. By leveraging

parallelized tensor operations to evaluate massive populations simultaneously, the execution time of the GA grows at a substantially slower pace.

VI. CONCLUSION

This paper presented a novel network architecture designed to maintain reliable communication in scenarios where a direct source-destination link is unavailable. The proposed framework capitalizes on the combined application of caching and backscatter technologies integrated with multiple UBDs. A joint optimization strategy is adopted to simultaneously design the DTS ratio, UBD trajectories, and transmission power to maximize the total network throughput. Numerical results emphasize the design's effectiveness, especially in scenarios lacking multiple UBDs or optimized total transmission power configurations. The BCD and GA offer unique strengths in solving high-dimensional non-convex optimization problems.

While this study established rigorous theoretical upper bounds and robust simulation frameworks, empirical validation in real-world physical scenarios remains a critical next step. Deploying a multi-UAV swarm with active SWIPT arrays and microsecond-level DTS circuitry introduces severe hardware synchronization challenges and hardware impairments. Future research will focus on bridging this gap by implementing the proposed algorithms on edge-enabled testbeds to quantify the deployment penalties. In practical deployments, imperfect channel state information (CSI) severely degrades the reliability of optimization solvers. To address this, a highly promising approach involves an adaptive DTS that leverages Deep Q-Learning, which could be trained to causally observe the instantaneous received signal strength indicators and predict localized energy deficits to maintain robust connectivity.

REFERENCES

- [1] K. Teixeira, G. Miguel, H. S. Silva, and F. Madeiro, "A survey on applications of unmanned aerial vehicles using machine learning," *IEEE Access*, vol. 11, pp. 117 582–117 621, 2023.
- [2] J. Zhang, J. Cui, H. Zhong, I. Bolodurina, and L. Liu, "Intelligent drone-assisted anonymous authentication and key agreement for 5G/B5G vehicular ad-hoc networks," *IEEE Trans. Netw. Sci. Eng.*, vol. 8, no. 4, pp. 2982–2994, 2021.
- [3] A. Gao, Z. Shao, Y. Hu, and W. Liang, "Joint trajectory and energy efficiency optimization for multi-UAV assisted offloading," in *Proc. IGARSS*, 2022.
- [4] Z. Na, C. Ji, B. Lin, and N. Zhang, "Joint optimization of trajectory and resource allocation in secure UAV relaying communications for internet of things," *IEEE Internet Things J.*, vol. 9, no. 17, pp. 16 284–16 296, 2022.
- [5] A. Mondal, D. Mishra, G. Prasad, and A. Hossain, "Joint optimization framework for minimization of device energy consumption in transmission rate constrained UAV-assisted IoT network," *IEEE Internet Things J.*, vol. 9, no. 12, pp. 9591–9607, 2022.
- [6] Z. Na, C. Ji, B. Lin, and N. Zhang, "IRS-assisted laser-powered UAV energy harvesting for IoT networks," *IEEE Internet Things J.*, vol. 11, no. 5, pp. 7890–7901, 2024.
- [7] M. A. Jamshed and F. Ayaz, "Green UAV-enabled internet-of-things network with AI-assisted NOMA for disaster management," *IEEE Internet Things J.*, vol. 10, no. 17, pp. 6500–6514, 2023.
- [8] H. Luo, Q. Zhang, H. Yu, G. Sun, and S. Xu, "Symbiotic PBFT consensus: Cognitive backscatter communications-enabled wireless PBFT consensus," in *Proc. GLOBECOM*, 2023.
- [9] X. Zhang, W. Liu, N. Huang, and Z. Xu, "Backscattering interference channel characteristics in full-duplex underwater optical wireless communication," in *Proc. ICCSN*, 2023.

- [10] S. Sood, "An overview of backscatter communication technique for performing wireless sensing in green communication networks," in *Proc. PEEIC*, 2023.
- [11] G. Yang, R. Dai, and Y.-C. Liang, "Energy-efficient uav backscatter communication with joint trajectory design and resource optimization," *IEEE Trans. Wireless Commun.*, vol. 20, no. 2, pp. 926–941, 2021.
- [12] W. Lu, Y. Ding, Y. Gao, S. Hu, Y. Wu, N. Zhao, and Y. Gong, "Resource and trajectory optimization for secure communications in dual unmanned aerial vehicle mobile edge computing systems," *IEEE Trans. Industr. Inform.*, vol. 18, no. 4, pp. 2704–2713, 2022.
- [13] Z. Guan, S. Wang, L. Gao, and W. Xu, "Energy-efficient UAV communication with 3D trajectory optimization," in *Proc. ICC*, 2021.
- [14] H. Tian, M. Yan, L. Dai, and P. Yang, "Joint communication and computation resource scheduling of a solar-powered UAV-assisted communication system for platooning vehicles," in *Proc. ICME*, 2023.
- [15] L. Xie, X. Cao, J. Xu, and R. Zhang, "Uav-enabled wireless power transfer: A tutorial overview," *IEEE Trans. Green Commun. Netw.*, vol. 5, no. 4, pp. 2042–2064, 2021.
- [16] Y. Liu, K. Xiong, Y. Lu, Q. Ni, P. Fan, and K. B. Letaief, "UAV-aided wireless power transfer and data collection in rician fading," *IEEE J. Sel. Areas Commun.*, vol. 39, no. 10, pp. 3097–3113, 2021.
- [17] H. Ren, Z. Zhang, Z. Peng, L. Li, and C. Pan, "Energy minimization in ris-assisted uav-enabled wireless power transfer systems," *IEEE Internet Things J.*, vol. 10, no. 7, pp. 5794–5809, 2023.
- [18] D. N. K. Jayakody, T. D. P. Perera, A. Ghayeb, and M. O. Hasna, "Self-energized UAV-assisted scheme for cooperative wireless relay networks," *IEEE Trans. Veh. Technol.*, vol. 69, no. 1, pp. 578–592, 2020.
- [19] H. Yan, Y. Chen, and S.-H. Yang, "UAV-enabled wireless power transfer with base station charging and UAV power consumption," *IEEE Trans. Veh. Technol.*, vol. 69, no. 11, pp. 12 883–12 896, 2020.
- [20] M. Sheng, J. Liu, R. Zhang, G. Li, and W. Xu, "UAV-assisted mobile edge computing with backscatter-aided IoT devices: Task scheduling and resource allocation," *IEEE Internet Things J.*, vol. 10, no. 6, pp. 4942–4955, 2023.
- [21] F. Fazel, J. Abouei, M. Jaseemuddin, A. Anpalagan, and K. N. Plataniotis, "Secure throughput optimization for cache-enabled multi-UAVs networks," *IEEE Internet Things J.*, vol. 9, no. 10, pp. 7783–7801, 2022.
- [22] Y. Liu, C. Yang, X. Chen, and F. Wu, "Joint hybrid caching and replacement scheme for UAV-assisted vehicular edge computing networks," *IEEE Trans. Intell. Veh.*, vol. 9, no. 1, pp. 866–878, 2024.
- [23] A. Masood, T.-V. Nguyen, T. P. Truong, and S. Cho, "Content caching in HAP-assisted multi-UAV networks using hierarchical federated learning," in *Proc. ICTC*, 2021, pp. 1160–1162.
- [24] R. Zhang, R. Lu, X. Cheng, N. Wang, and L. Yang, "A UAV-enabled data dissemination protocol with proactive caching and file sharing in V2X networks," *IEEE Trans. Commun.*, vol. 69, no. 6, pp. 3930–3942, 2021.
- [25] Z. Zhao, X. Zhang, H. Li, K. Deng, and K. Wu, "Joint cooperative caching and power control for UAV-enabled vehicular IoT networks," *IEEE Internet Things J.*, vol. 11, no. 3, pp. 2190–2204, 2024.
- [26] M. Hua, L. Yang, C. Li, Q. Wu, and A. L. Swindlehurst, "Throughput maximization for UAV-aided backscatter communication networks," *IEEE Trans. Commun.*, vol. 68, no. 2, pp. 1254–1270, 2020.
- [27] D.-H. Tran, S. Chatzinotas, and B. Ottersten, "Throughput maximization for backscatter- and cache-assisted wireless powered UAV technology," *IEEE Trans. Veh. Technol.*, vol. 71, no. 5, pp. 5187–5202, 2022.
- [28] Y. Du, Z. Chen, J. Hao, and Y. Guo, "Joint optimization of trajectory and communication in multi-UAV assisted backscatter communication networks," *IEEE Access*, vol. 10, pp. 40 861–40 871, 2022.
- [29] X. Jiang, M. Sheng, N. Zhao, J. Liu, D. Niyato, and F. R. Yu, "Outage analysis of UAV-aided networks with underlaid ambient backscatter communications," *IEEE Trans. Wireless Commun.*, vol. 22, no. 11, pp. 7492–7505, 2023.
- [30] B. Adhikari, A. S. Khwaja, M. Jaseemuddin, A. Anpalagan, and A. Nallanathan, "Energy efficient RIS-assisted UAV networks using twin delayed DDPG technique," *IEEE Trans. Wireless Commun.*, vol. 23, no. 12, pp. 18 423–18 439, 2024.
- [31] L. Zhang, F. Wen, Q. Zhang, G. Gui, H. Sari, and F. Adachi, "Constrained multiobjective decomposition evolutionary algorithm for UAV-assisted mobile edge computing networks," *IEEE Internet Things J.*, vol. 11, no. 22, pp. 36 673–36 687, 2024.
- [32] B. Li, S. Tripathi, S. Hosain, R. Zhang, M. Wang, and J. Xie, "When learning meets dynamics: Distributed user connectivity maximization in UAV-based communication networks," *IEEE Trans. Cogn. Commun. Netw.*, pp. 1–1, 2025.
- [33] Y. Yuan, L. Lei, T. X. Vu, S. Chatzinotas, S. Sun, and B. Ottersten, "Energy minimization in UAV-aided networks: Actor-critic learning for constrained scheduling optimization," *IEEE Trans. Veh. Technol.*, vol. 70, no. 5, pp. 5028–5042, 2021.
- [34] T. Van Chien, B. T. Duc, N. X. Tung, V. D. Nguyen, W. Khalid, S. Chatzinotas, and L. Hanzo, "Single-and multi-objective stochastic optimization for next-generation networks in the generative AI and quantum computing era," *arXiv preprint arXiv:2601.02175*, 2026.
- [35] M. Ravan, F. S. Tabataba, M. S. Fazel, and H. Yanikomeroglu, "Enhancing spectral efficiency: the impact of RIS elements association on multi-user cell-free wireless networks," *IEEE Open Journal of the Communications Society*, vol. 6, pp. 1895 – 1913, 2025.
- [36] J. Huangfu, Z. Song, T. Hou, A. Li, Y. Liu, A. Nallanathan, and K.-K. Wong, "Performance analysis of fluid antenna system under spatially-correlated Rician fading channels," *IEEE Trans. Wireless Commun.*, vol. 25, pp. 1394 – 1407, 2025.
- [37] B. Lyu, C. You, Z. Yang, and G. Gui, "The optimal control policy for RF-powered backscatter communication networks," *IEEE Trans. Veh. Technol.*, vol. 67, no. 3, pp. 2804–2808, 2018.
- [38] Y. Zeng, J. Xu, and R. Zhang, "Energy minimization for wireless communication with rotary-wing UAV," *IEEE Trans. Wireless Commun.*, vol. 18, no. 4, pp. 2329–2345, 2019.
- [39] S. Xiao, H. Guo, and Y.-C. Liang, "Resource allocation for full-duplex-enabled cognitive backscatter networks," *IEEE Trans. Wireless Commun.*, vol. 18, no. 6, pp. 3222–3235, 2019.
- [40] X. Kang, Y.-C. Liang, and J. Yang, "Riding on the primary: A new spectrum sharing paradigm for wireless-powered IoT devices," *IEEE Trans. Wireless Commun.*, vol. 17, no. 9, pp. 6335–6347, 2018.
- [41] S. Gong, X. Huang, J. Xu, W. Liu, P. Wang, and D. Niyato, "Backscatter relay communications powered by wireless energy beamforming," *IEEE Trans. Commun.*, vol. 66, no. 7, pp. 3187–3200, 2018.
- [42] I. S. Gradshteyn and I. M. Ryzhik, *Table of integrals, series, and products*. Academic press, 2014.
- [43] M. Hong, M. Razaviyayn, Z.-Q. Luo, and J.-S. Pang, "A unified algorithmic framework for block-structured optimization involving big data: With applications in machine learning and signal processing," *IEEE Signal Process. Mag.*, vol. 33, no. 1, pp. 57–77, 2016.
- [44] S. P. Boyd and L. Vandenberghe, *Convex optimization*. Cambridge university press, 2004.
- [45] S. Boyd, "Advances in convex optimization: Interior-point methods, cone programming, and applications," in *Proc. CDC*, 2002.
- [46] G. Zhang, Q. Wu, M. Cui, and R. Zhang, "Securing UAV communications via joint trajectory and power control," *IEEE Trans. Wireless Commun.*, vol. 18, no. 2, pp. 1376–1389, 2019.
- [47] M. Grant, S. Boyd, and Y. Ye, "CVX users' guide," 2009.
- [48] S. Yin, L. Li, and F. R. Yu, "Resource allocation and basestation placement in downlink cellular networks assisted by multiple wireless powered UAVs," *IEEE Trans. Veh. Technol.*, vol. 69, no. 2, pp. 2171–2184, 2020.
- [49] Z. Chen and X. Wang, "Decentralized computation offloading for multi-user mobile edge computing: A deep reinforcement learning approach," *EURASIP J. Wirel. Commun. Netw.*, vol. 2020, no. 1, p. 188, 2020.
- [50] V. Roberge, M. Tarbouchi, and G. Labonté, "Fast genetic algorithm path planner for fixed-wing military UAV using GPU," *IEEE Trans. Aerosp. Electron. Syst.*, vol. 54, no. 5, pp. 2105–2117, 2018.